

See discussions, stats, and author profiles for this publication at: <https://www.researchgate.net/publication/325793956>

Urban tree health assessment using airborne hyperspectral and LiDAR imagery

Article · December 2018

DOI: 10.1016/j.jag.2018.05.021

CITATIONS

39

READS

776

5 authors, including:



Jeroen Degerickx

Flemish Institute for Technological Research

16 PUBLICATIONS 175 CITATIONS

[SEE PROFILE](#)



Dar A. Roberts

University of California, Santa Barbara

408 PUBLICATIONS 22,527 CITATIONS

[SEE PROFILE](#)



Martin Hermý

KU Leuven

463 PUBLICATIONS 22,227 CITATIONS

[SEE PROFILE](#)



Ben Somers

KU Leuven

178 PUBLICATIONS 3,831 CITATIONS

[SEE PROFILE](#)

Some of the authors of this publication are also working on these related projects:



Herb layer recovery in post-agricultural forests [View project](#)



Three decades of anthropogenic fire activity in a Neotropical agricultural frontier [View project](#)

Urban tree health assessment using airborne hyperspectral and LiDAR imagery

Degerickx, J. ^{a *}, Roberts, D.A. ^b, McFadden, J. P. ^b, Hermy, M. ^a, Somers, B. ^a

^a Division of Forest, Nature and Landscape, KU Leuven, Leuven, Belgium.

^b Department of Geography, University of California Santa Barbara, CA, 93106, United States.

* Corresponding author: jeroen.degerickx@kuleuven.be; Tel.: +32 16 37 21 94

Link to published version: <https://doi.org/10.1016/j.jag.2018.05.021>

Abstract

Urban trees provide valuable ecosystem services but are at the same time under continuous pressure due to unfavorable site conditions. In order to better protect and manage our natural capital, urban green managers require frequent and detailed information on tree health at the city wide scale. In this paper we developed a workflow to monitor tree defoliation and discoloration of broadleaved trees in Brussels, Belgium, through the combined use of airborne hyperspectral and LiDAR data. Individual trees were delineated using an object-based tree detection and segmentation algorithm primarily based on LiDAR data with an average accuracy of 91 %. We constructed Partial Least Squares Regression (PLSR) models to derive tree chlorophyll content (RMSE = 2.8 $\mu\text{g}/\text{cm}^2$; $R^2 = 0.77$) and Leaf Area Index (LAI; RMSE = 0.5; $R^2 = 0.66$) from the average canopy spectrum. Existing spectral indices were found to perform significantly worse (RMSE > 7 $\mu\text{g}/\text{cm}^2$ and > 1.5 respectively), mainly due to contamination of tree spectra by neighboring background materials. In the absence of local calibration data, the applicability of PLSR to other areas, sensors and tree species might be limited. Therefore, we identified the best performing/least sensitive spectral indices and proposed a simple pixel selection procedure to reduce disturbing background effects. For LAI, laser penetration metrics derived from LiDAR data attained comparable accuracies as PLSR and were suggested instead. Detection of healthy and unhealthy trees based on remotely sensed tree properties matched reasonably well with a more traditional visual tree assessment (93% and 71% respectively). If combined with early tree stress detection methods, the proposed methodology would constitute a solid basis for future urban tree health monitoring programs.

Highlights

- Chlorophyll content and LAI are derived for individual urban trees
- Partial Least Squares Regression outperforms spectral indices
- Interference by background materials is significant in urban areas
- Remote sensing holds great potential for urban tree health monitoring

Keywords: remote sensing, tree segmentation, chlorophyll, leaf area index, spectral indices, partial least squares regression

1 Introduction

Urban trees and forests are known to provide a wide range of ecosystem services (e.g. cooling, air filtering, water interception, recreation), thereby significantly improving the quality of life for urban residents (Bolund and Hunhammar, 1999; Salmond et al., 2016). At the same time, urban trees are under continuous pressure due to several factors that negatively affect their health (Berrang et al., 1985). Compared to the surrounding rural areas, urban environments are characterized by high peak temperatures (Cregg and Dix, 2001), high concentrations of air pollution and poor soil conditions due to human activities. Urban soils typically contain high amounts of inert construction materials, pollutants and de-icing salts, are characterized by high bulk densities and poor soil structure due to soil compaction and hence support little biological activity, in turn leading to low organic matter content (Czerniawska-Kusza et al., 2004; Day and Bassuk, 1994; Scharenbroch et al., 2005). All these factors increase the risk of nutrient and water stress, in turn deteriorating a tree's metabolism and growth and decreasing its ability to provide ecosystem services. Particularly low available rooting space due to soil compaction has been found to negatively affect urban tree condition (Day and Bassuk, 1994; Sanders and Grabosky, 2014; Scharenbroch et al., 2017). In addition, poor site conditions increase the risk of infestation by insects and diseases (Cregg and Dix, 2001). Severe tree health issues may eventually lead to tree stability loss, in turn threatening public safety (Lonsdale, 1999). Given their high value to society and the high pressure they are experiencing, urban trees should be carefully managed, including prevention, restoration and replacement of dead or diseased trees. To facilitate this, professional green managers ideally require frequent, reliable and spatially-explicit information on the health status of all trees under their care. Traditionally, tree health is monitored using the visual tree assessment (VTA) method (Mattheck and Breloer, 1994), applied in-situ by trained tree experts. Although this method has already been successfully used in many cities (Fink, 2009), it is affected by a certain degree of subjectivity, provides mostly qualitative information and is limited in spatial extent and temporal frequency to time and labor constraints of tree experts. Remote sensing technology has the potential to deliver quantitative, spatially continuous information covering entire cities at once and can be easily replicated through time.

Tree health research employing remote sensing data has been dominated by forestry studies linking vegetation indices like NDVI (Normalized Difference Vegetation Index; Rouse et al., 1973), mostly derived from multispectral satellite data, to different tree health aspects like defoliation (Royle and Lathrop, 1997; Wang et al., 2010). Aside from estimating vegetation abundance and cover (Van De Voorde et al., 2008), the potential of this coarse (10 – 30 m) multispectral data for urban vegetation studies is limited by the high abundance of mixed pixels in urban scenes compared to more uniform forest ecosystems. The presence of background materials within a pixel negatively affects the calculation of vegetation indices (Somers et al., 2009b; van Beek et al., 2015). Researchers have therefore turned to color infrared imagery, sacrificing spectral detail in favor of fine spatial resolution (< 1m), for urban tree health mapping (Sari and Kushardono, 2016; Xiao and McPherson, 2005). Such imagery however only provides general measures of greenness (such as NDVI), typically sensitive to multiple vegetation characteristics at once (e.g. chlorophyll content and biomass), and hence enable us to locate problematic trees but without identifying the underlying causes. Different types of stress trigger different physiological reactions in trees (Günthardt-Goerg and Vollenweider, 2007), which are eventually expressed visually either via leaf loss (drought, frost, insect damage) or via changes in leaf color (nutrient stress, diseases). Both variables (defoliation and discoloration) are often used in conjunction as tree health indicators (Lakatos et al., 2014; Stone et al., 2000) and can, from a remote sensing perspective, objectively be estimated by respectively determining Leaf Area Index (LAI) and chlorophyll content. Airborne hyperspectral data provides the spectral detail required to derive these individual tree characteristics (e.g. Delalieux et al., 2008; Delegido et al., 2014). Its lower spatial

resolution (typically 2-4 m) can be compensated through fusion with airborne LiDAR data, providing highly detailed structural information. The added value of the LiDAR component for urban tree health assessment lies in its potential to estimate LAI (Alonzo et al., 2015; Klingberg et al., 2017; Morsdorf et al., 2006; Oshio et al., 2015) and to delineate individual tree objects in a highly accurate way (Alonzo et al., 2014; Zhao et al., 2017; Zhen et al., 2016).

The main objective of this study was to develop a workflow to assess urban tree health in a quick and cost-effective way using a combination of airborne hyperspectral and LiDAR data as an alternative to the currently established VTA approach. Our workflow comprised three steps: (1) detailed detection and delineation (segmentation) of individual trees using airborne LiDAR data, (2) determination of chlorophyll content and LAI of each individual tree from airborne hyperspectral and LiDAR data and (3) integration of these two variables into an objective tree health indicator. In this paper, an unhealthy tree is defined as a tree featuring a decreased metabolism, visually expressed by significant defoliation and/or leaf discoloration when compared to other trees from the same species. The approach was tested on a set of trees in the city of Brussels, Belgium. For the extraction of tree properties from hyperspectral data we compared the performance of spectral indices (a biophysically based approach) versus Partial Least Squares Regression (PLSR; a regression approach relying on local calibration data). PLSR was preferred here over other machine learning approaches as it is widely recognized as one of the standardized approaches to retrieve canopy biochemistry from hyperspectral data, uses the entire spectrum to predict the variable of interest and results in a set of meaningful and easily interpretable regression coefficients allowing to identify the most important spectral zones with regard to this variable (Asner et al., 2011; Martin et al., 2008; Meerdink et al., 2016; Singh et al., 2015; Townsend et al., 2003). Many different spectral indices have already been developed to derive chlorophyll content (e.g. Dash and Curran, 2004; Daughtry et al., 2000; Gitelson et al., 2003; Sims and Gamon, 2002) and to a lesser extent LAI (Delalieux et al., 2008). With the exception of the NAOC index (Delegido et al., 2014), all of these indices were designed for relatively homogeneous forest canopies or plantations. An important objective of this study was, therefore, to test which of the existing indices can be safely applied to the complex urban environment, with its high abundance of man-made materials. We additionally tested a strategy to minimize background effects by gradually eliminating contaminated or non-pure tree pixels from the analysis. Although many studies exist on deriving individual tree properties from remote sensing data, to our knowledge this study was the first attempt to integrate these properties into an objective health indicator specifically for urban trees.

2 Data

2.1 Airborne hyperspectral data

On June, 30 2015 a hyperspectral image was acquired over the city of Brussels, Belgium using the Airborne Prism Experiment (APEX) sensor mounted in an airplane. The flight took place around solar noon at an altitude of 3600 m above sea level. APEX records the spectral response in 285 spectral bands within the 412 – 2431 nm range, of which 218 were retained for analysis after removal of atmospheric absorption bands (412 – 450 nm, 1340 – 1500 nm, 1760 – 2020 nm, 2350-2431 nm). Image pre-processing was done using an automated processing chain at the Flemish Institute for Technological Research (Biesemans et al., 2007), consisting of geometric correction via direct georeferencing (Vreys et al., 2016), projection in the Belgian Lambert 72 coordinate system and atmospheric correction using a MODTRAN4 radiative transfer model (Berk et al., 1999; Sterckx et al., 2016). The resulting image had a spatial resolution of 2 m and mainly covered the Eastern part of the Brussels capital area (Figure 1), comprising a wide range of urban structure types (i.e. dense and sparse residential, commercial and urban green zones).

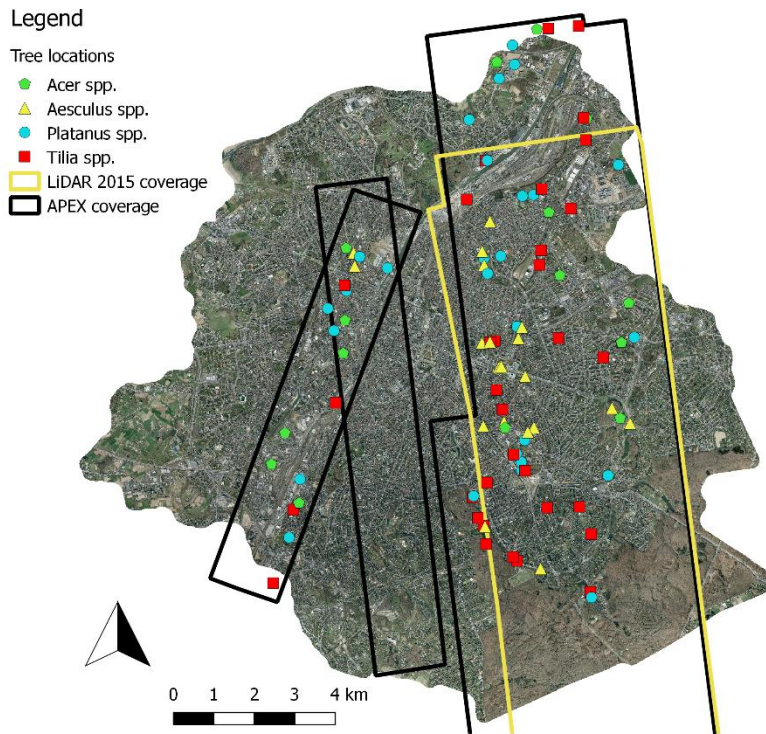


Figure 1: Location of urban trees used in this study within the Brussels Capital Region, Belgium, and in relation to the coverage of the APEX hyperspectral dataset (black rectangles), LiDAR 2015 (yellow rectangle) and LiDAR 2012 datasets (entire region).

2.2 Airborne LiDAR data and derived surface models

The eastern part of our study area was covered by an airborne LiDAR dataset collected in Summer 2015 by Aerodata Surveys Nederland BV (yellow rectangle in Figure 1) with an average point density of 15 points/m². For the remainder of the study area not covered by the 2015 dataset, we relied on a LiDAR dataset acquired in winter 2012 over the entire Brussels Capital Region with an average point density of 35 points/m² (data provided by the Brussels Regional Informatics Centre). For both datasets a digital terrain model (DTM; elevation of ground level) and canopy height model (CHM; height of objects) were derived at a resolution of 0.25 m using LAsTools software. The processing chain included the detection and removal of noisy returns, the detection of ground returns, creation of the DTM through interpolation, deriving height of all non-ground returns and creation of a CHM by extracting the maximum height for each cell (full code in Supplement I).

2.3 Urban tree dataset

2.3.1 Tree selection

Validation data were collected for a total of 118 trees, selected by stratified random sampling across our study area (Figure 1). We only considered trees located on public property and focused on the four most dominant tree genera occurring along public roads in the city of Brussels, i.e. *Acer* (mainly *A. pseudoplatanus* and *A. platanoides*; $n = 24$), *Aesculus* (*A. hippocastanum*; $n = 26$), *Platanus* (*P. x acerifolia*; $n = 30$) and *Tilia* (mainly *T. x euchlora* and *T. x europaea*; $n = 38$). The study area was first stratified into four urban structure types (dense residential, sparse residential, industrial and urban green zone) based on the type and density of buildings, derived visually from an orthophoto. We then randomly selected our trees during several field visits to different zones and made sure to include trees of various sizes, health conditions and spatial contexts (park versus street). The trees' locations were recorded using a Garmin GPSMAP 64S (± 3 m) and their context was meticulously described allowing

their identification on a 7.5 cm RGB orthophoto. Tree height was measured using a Silva CM-360 clinometer.

2.3.2 Chlorophyll

Based on an independent tree leaf dataset, we established a relation between leaf spectral measurements and leaf chlorophyll content (Gitelson et al., 2003; Sims and Gamon, 2002). The dataset comprised 31 *Platanus* leaves and 26 *Aesculus* leaves collected in Leuven (Belgium) from 12 different individuals showing a clear gradient in tree health. After harvesting, leaves were stored in an ice chest and transported to the lab where three spectra per leaf (350 – 2500 μm) were measured using a SpectraVista spectroradiometer (SVC HR1024) equipped with a leaf clip containing an internal illumination source. Chlorophyll content was determined by dissolving a known area fraction of the leaf in (80:20) acetone- H_2O solvent (as suggested by Porra, 2002), measuring the reflectance of the resulting fluid in a spectrophotometer and applying the equations from Lichtenthaler (1987). A PLSR model (Helland et al., 2006) was constructed by randomly dividing the leaf data into 80% calibration and 20% validation sets and running PLSR using 5 components (latter based on evaluation of the PRESS statistic). This process was repeated a thousand times and the resulting model coefficients were averaged to yield the final model ($R^2 = 0.82$; RMSE = 4.40). By comparing the performance of this pooled model with two species-specific models (trained only with data from the respective species), we concluded the species effect to be negligible for chlorophyll prediction of these deciduous broadleaf trees. Therefore, we used the pooled PLSR model to estimate the true chlorophyll content of each tree in the Brussels dataset based on spectral measurements (see above) of twenty individual leaves per tree.

2.3.3 Leaf Area Index (LAI)

The LAI of each individual tree was measured using two different methods, which were averaged to obtain one value per tree. The first method was based on a set of four upward facing photographs taken from below the canopy (one in each of the four cardinal directions) at a distance of 1 m from the stem and a height of 1 m above the ground surface using a Canon EOS 5D camera. After manually cropping the images for removing unwanted features (e.g. buildings), Gap Light Analyzer software was used to derive LAI. The second method made use of the Sunscan system (Type SS1-COM-R4), consisting of two sensors (one BF5 sunshine sensor placed outside the canopy and the actual Sunscan sensor positioned underneath the canopy) simultaneously measuring incident photosynthetically active radiation. LAI was subsequently derived based on the fraction of radiation transmitted through the canopy (Wirion et al., 2017).

2.3.4 Visual tree assessment (VTA)

The health status of all trees was assessed on site by two independent researchers using the FAO guidelines for the assessment of forest crown condition (Lakatos et al., 2014). Both defoliation and discoloration of leaves were estimated on a 0-3 scale through comparison to a healthy reference tree. The final damage score per tree was obtained through integration of the two variables (Table 1). As the amount of foliage (and hence LAI) of a healthy tree varies significantly depending on its size, we grouped our data not only by species, but also into two size classes (lower and higher than 13 m). For each group, we visually selected 2-3 healthy trees from our sampled tree dataset that served as a reference to estimate defoliation and discoloration.

Table 1: Final damage score of an individual tree as a function of defoliation and discoloration percentages and scores. Adopted from Lakatos et al., 2014.

| Defoliation | | Discoloration | | | |
|-------------|---|---------------|-----------|-----------|------------|
| | | 0 – 10 % | 10 – 25 % | 25 – 60 % | 60 – 100 % |
| 0 – 10 % | 0 | 0 | 0 | 1 | 2 |
| 10 – 25 % | 1 | 1 | 1 | 2 | 2 |
| 25 – 60 % | 2 | 2 | 2 | 3 | 3 |
| 60 – 100 % | 3 | 3 | 3 | 3 | 3 |

3 Methodology

3.1 Overview of tree health workflow

Our workflow to derive tree health information from airborne hyperspectral and LiDAR data is summarized in Figure 2. LiDAR pre-processing has already been covered in Section 2.2. Each of the next steps will be thoroughly discussed in the following sections.

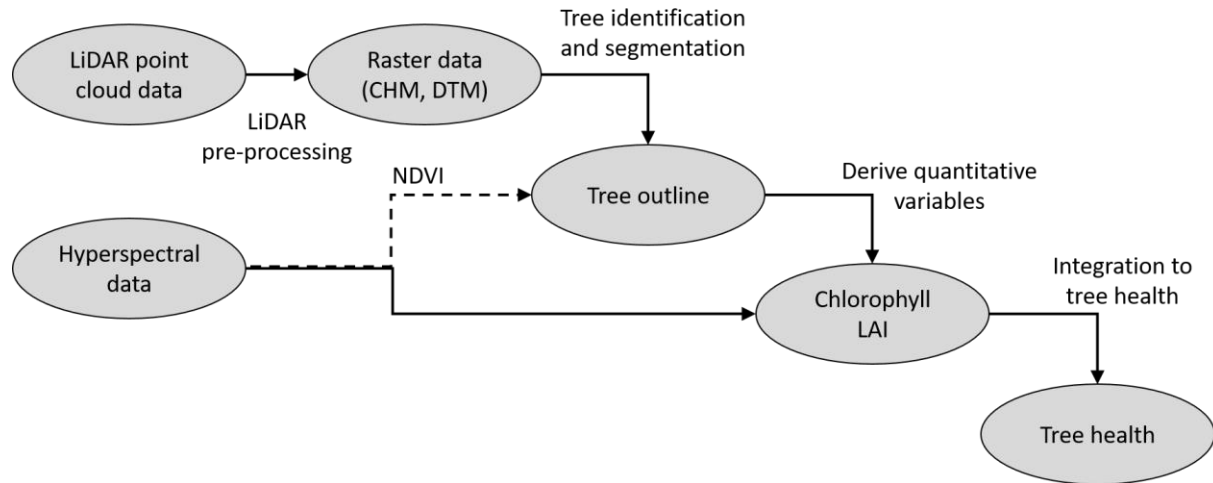


Figure 2: Overview of the proposed workflow to derive tree health information from airborne hyperspectral and LiDAR data.

3.2 Tree identification and segmentation

We developed an object-based tree classification algorithm in eCognition software (see Supplement 2 for the detailed algorithm), mainly relying on a LiDAR based tree index proposed by O’Neil-Dunne et al. (2014) (Equation 1; Figure 3). This index was calculated for our study area with a spatial resolution of 25 cm. All objects taller than 3 m and having a tree index > 1 were initially labeled as trees (Figure 44 a,b,c). Building edges however tended to have high tree index values, causing them to be wrongly classified as trees (Figure 4 c). This problem was solved by reclassifying tree or unclassified objects with similar NDVI values compared to neighboring building objects (Figure 4d,e). In cases where multiple trees were spatially connected into large asymmetric tree objects, we used a watershed segmentation algorithm in order to isolate individual trees (Figure 4f).

$$Tree\ index = H_{first} - H_{last} \quad [Equation\ 1]$$

where H_{first} and H_{last} represent the height of the first and last LiDAR return in a pixel relative to the ground surface.

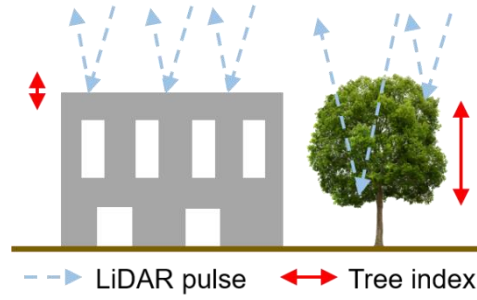


Figure 3: Illustration of the concept of the tree index (Equation 1) derived from airborne LiDAR data. Laser pulses can penetrate tree canopies, but cannot penetrate buildings. For the former, the difference between first and last return will be much higher compared to the latter.

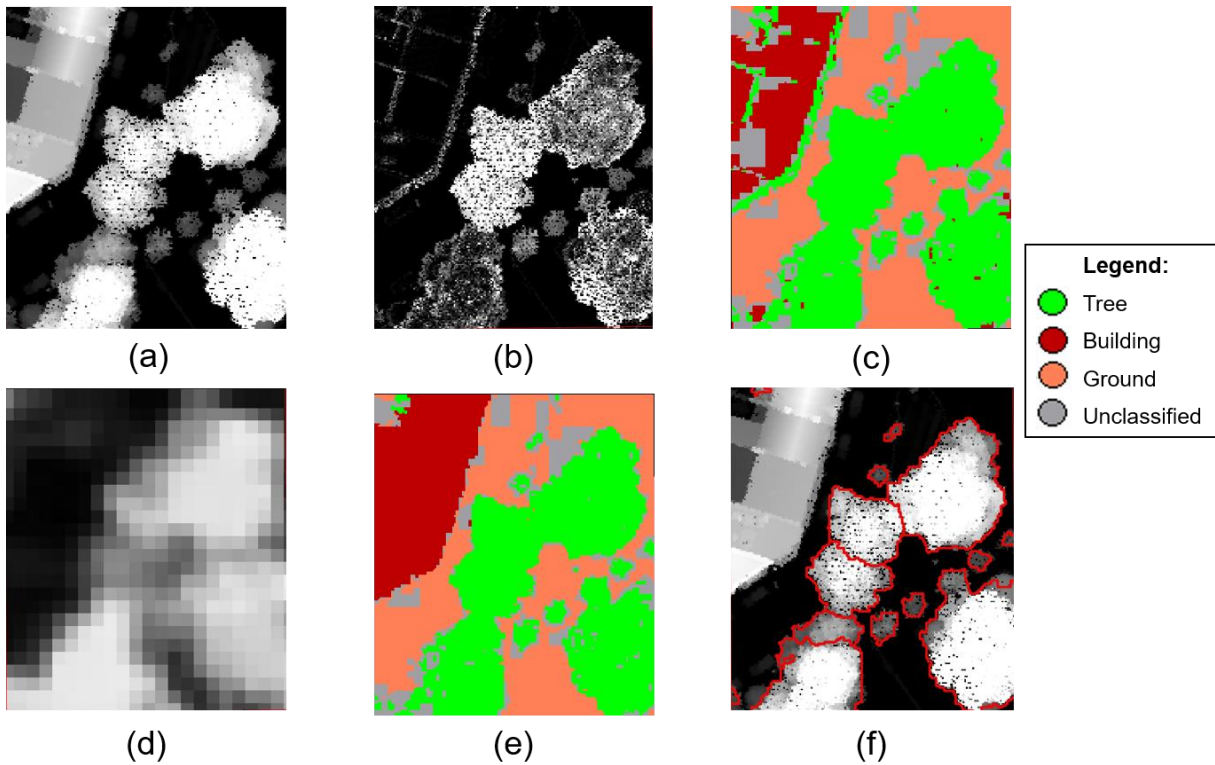


Figure 4: Illustration of the tree identification and segmentation algorithm. (a) Canopy height model (CHM; 25 cm resolution); (b) tree index (Equation 1; 25 cm resolution); (c) initial classification based on CHM and tree index, note that edges of buildings are wrongly classified as trees due to high tree index values; (d) NDVI derived from APEX data (2 m resolution); (e) corrected classification based on NDVI thresholds, which resolved the misclassification of building edges; (f) final tree segments after watershed segmentation (red polygons).

The accuracy of the tree identification and segmentation algorithm was evaluated by directly comparing the resulting polygons to manually-drawn tree polygons based on visual interpretation of the CHM and high-resolution RGB imagery (7.5 cm resolution). The fraction of overlapping area between the two sets was calculated both from the viewpoint of the reference and segmentation result (see Formulas in Table 2 and Zhao et al., 2017). Based on both fractions, segmentation results were classified as a good match, over- or underestimated and mismatch (Table 2). The average fraction of overlapping area was used as a general measure of accuracy.

3.3 Deriving quantitative variables: chlorophyll content and LAI

After individual tree crown delineation, the spectral information of each tree segment was extracted from the APEX imagery and was used to derive chlorophyll content and LAI. By computing the average

signal per tree object, we specifically accounted for intra-crown variability. This is in contrast to Delegido et al. (2014), who used only the central pixel per tree crown. In this study we compared two conceptually different approaches for tree property extraction, i.e. spectral indices (Section 3.3.1) and PLSR (Section 3.3.2). In addition, we also tested the potential of LiDAR data to derive LAI (Section 3.3.3). Given the highly heterogeneous nature of urban environments, combined with a high material diversity and hence high spectral complexity (Heiden et al., 2007), urban tree spectra are especially prone to contamination by background materials. Despite the 2 m spatial resolution, mixed pixels still occur, particularly near tree edges and in case of low foliage density. Signal contamination is additionally aggravated by multiple scattering effects, resulting in complex nonlinear spectral mixtures (Somers et al., 2009a). Moreover, small errors in the tree identification and segmentation procedure or a slight geometric mismatch between the hyperspectral and LiDAR datasets can cause pixels not containing any vegetation to be wrongly labeled as part of a tree canopy (Figure 5). We developed a multi-criteria pixel selection procedure to minimize these background effects (Section 3.3.4). Finally, the sensitivity of the different methods to remaining background contamination is assessed (Section 3.3.5).

3.3.1 Spectral indices

We tested a wide range of spectral indices for chlorophyll content and LAI (Table 3). The NAOC index is particularly worth mentioning since it was specifically designed for heterogeneous environments and has already been successfully applied in an urban context (Delegido et al., 2014). In addition to these existing indices, an optimized normalized index was designed using the OMNBR approach (Thenkabail et al., 2000). In this approach, all normalized vegetation indices were generated using every possible combination of two spectral bands and the one showing the highest correlation to the variable of interest was retained. A linear relation was fitted between each spectral index and measured chlorophyll/LAI, except for the NAOC index where we used a log-linear relation (Delegido et al., 2014).

3.3.2 Partial least squares regression (PLSR)

PLSR is a data fitting approach typically used in cases where more predicting variables are available compared to observations (in our case 218 spectral bands versus 118 trees available for calibration) and has been widely used to assess tree variables in forests based on hyperspectral data (Singh et al., 2015; Townsend et al., 2003). PLSR was applied as outlined in Section 2.3.2, i.e. by creating and subsequently averaging 1000 individual models (each based on a different random subset of calibration/validation data in a 80:20 ratio). This approach allowed us to assess the sensitivity of the model towards the actual calibration data used and to estimate model accuracy (Singh et al., 2015). Both a global (based on all data/all species) and species-specific PLSR models were generated for chlorophyll and LAI. The contribution of each spectral band to the final regression model, as expressed by the regression coefficients (or beta values), was used to identify the most relevant spectral zones for chlorophyll and LAI.

3.3.3 LAI from LiDAR

As an alternative to the use of spectral data, many studies have focused on extracting LAI from airborne LiDAR data via laser penetration metrics, including in urban areas (Alonzo et al., 2015; Klingberg et al., 2017; Oshio et al., 2015). Here, we briefly tested the potential of this approach on the 84 trees imaged by LiDAR in summer (Figure 1). For each of these crown objects, we extracted the number of first canopy returns and first and last ground returns using OPALS software, and used these numbers to calculate a specific laser penetration metric (LPM_{lasts} , formula specified in Alonzo et al., 2015). LPM_{lasts} was converted to LAI using an inverse logarithmic formula (Alonzo et al., 2015) and related to measured LAI using linear regression.

3.3.4 Dealing with background signals using canopy pixel selection

We developed a multi-criteria canopy pixel selection procedure (Figure 5) in order to detect and remove contaminated canopy pixels. The procedure first deleted all pixels which intersect with the tree crown border. Next, the NDVI and a newly developed grass index were calculated for each remaining pixel to estimate the contamination by man-made materials and grass respectively. The grass index was created based on the observation that grass spectra reach their maximum reflectance in the NIR region around 1050 nm, whereas in tree spectra, this peak is less pronounced or even lower compared to the reflectance around 805 nm (Figure 6; Equation 2). We used a conservative NDVI threshold of 0.3 in order to conserve unhealthy tree spectra and a grass index threshold (git) of 0.87 to distinguish grass (< git) from tree (> git) pixels. A test on two independent spectral libraries from the cities of Brussels (APEX 2015 dataset) and Berlin (3.6 m resolution HyMap data) (Degerickx et al., 2017) showed this approach to yield a total accuracy of 87.7 and 76.2% respectively for differentiating grass from tree pixels. The number of pure tree and grass spectra amounted to 486/255 for Brussels and 1265/1112 for Berlin. Finally, we removed all shaded canopy pixels using a brightness criterion: canopy pixels with a brightness value less than 75% of the maximum brightness within the canopy were discarded. After each stage of the canopy pixel selection procedure (no selection - edge removal - NDVI criterion - grass index criterion - brightness criterion) we computed the average canopy signal based on the remaining pixels per tree. By applying our chlorophyll and LAI retrieval methods (Sections 3.3.1 and 3.3.2) on each of these five resulting sets of canopy spectra, we tested the added value of our suggested background removal approach.

$$\text{Grass index} = \frac{R_{805}}{R_{1050}} \quad [\text{Equation 2}]$$

where R_x is the reflectance at wavelength x (in nm).

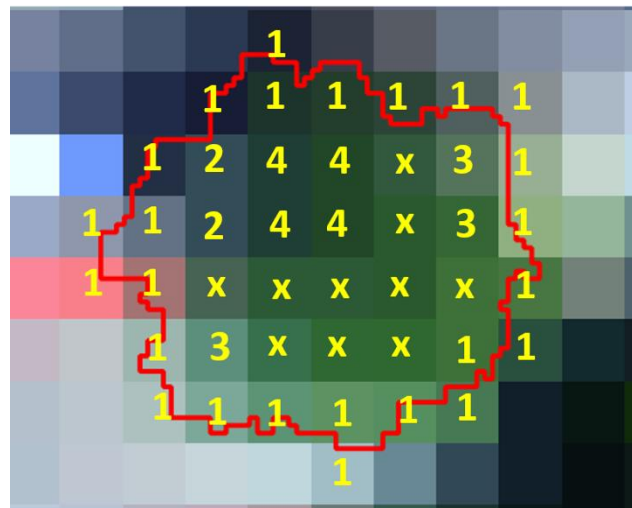


Figure 5: Illustration of canopy pixel selection procedure applied on one tree canopy. The red line shows the extent of the tree canopy as delineated by our tree segmentation algorithm. The pixels represent the true-color RGB version of the APEX image (2 m resolution). A geometric shift is visible between the LiDAR-based extent and the APEX image (non-vegetated pixels are included in the canopy on the left). Pixels containing a number/letter are originally included in the analysis. Pixels marked by a number are removed during canopy pixel selection (1 = edge pixels; 2 = non-vegetated pixels; 3 = grass pixels; 4 = shaded pixels). Pixels marked by "x" are the ones retained after the entire procedure.

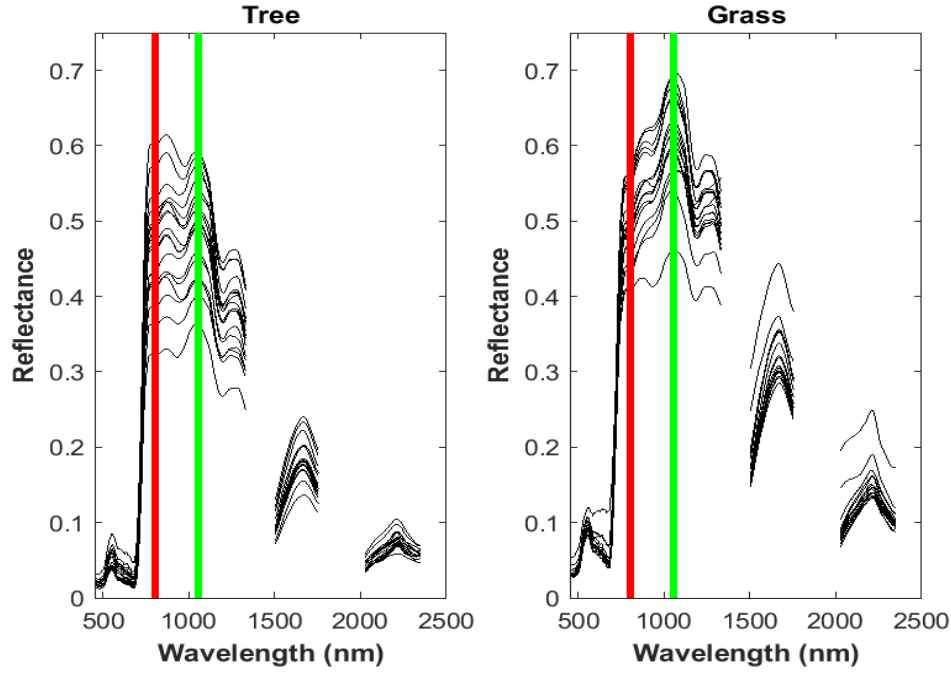


Figure 6: Twenty random tree spectra (left) and grass spectra (right) from our APEX 2015 dataset with an indication of the wavelengths used to calculate the grass index (805 nm = red; 1050 nm = green).

3.3.5 Sensitivity to background signals

In order to test for remaining sensitivity to background signals, we classified our trees in categories depending on their background material (impervious surface, bare soil, grass, shrubs, wood chips) and tested for significant differences in the prediction error of chlorophyll and LAI (Kruskal Wallis test). Additionally, we applied all indices and PLSR models on a random sample of pure spectra of common non-vegetated background materials in the city of Brussels (asphalt, concrete, soil and water; spectra drawn from the Brussels APEX spectral library from Degerickx et al. (2017)).

3.4 Integrated tree health indicator

The central concept behind this study was to move beyond the traditional assessment of vegetation properties from remote sensing data by integrating the acquired information into a meaningful and practical tree health indicator. Instead of visually estimating defoliation and discoloration (Lakatos et al., 2014, see Section 2.3.4), the two variables were derived by directly comparing LAI and chlorophyll values between the tree of interest and a set of healthy reference trees of the same species and within the same height category (Figure 7, Equation 3, Equation 4; see Section 2.3.4 for definition of reference trees). Defoliation, discoloration and final damage scores were defined using the thresholds mentioned in Table 1.

$$defoliation [\%] = \frac{\overline{LAI_{ref}} - LAI_{tree}}{\overline{LAI_{ref}}} * 100 \quad [Equation 3]$$

$$discoloration [\%] = \frac{\overline{chlor_{ref}} - chlor_{tree}}{\overline{chlor_{ref}}} * 100 \quad [Equation 4]$$

Where LAI = leaf area index, chlor = chlorophyll content, $\overline{X_{ref}}$ = average value of variable X for all reference trees, X_{tree} = variable X for tree of interest.

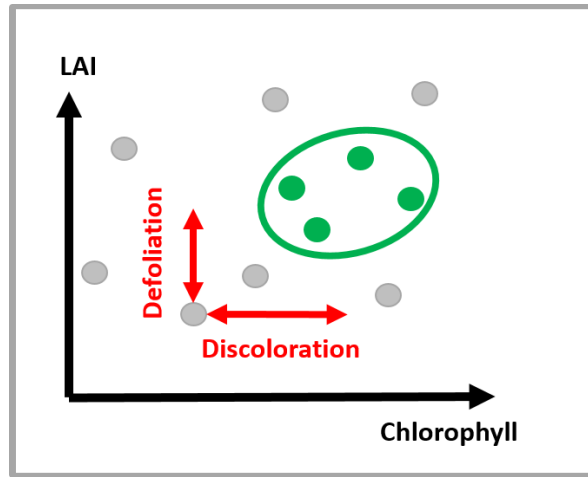


Figure 7: Conceptual representation of deriving defoliation and discoloration by comparing respectively LAI and chlorophyll content between a particular tree (grey dots) and a cluster of known healthy trees (green dots).

4 Results

4.1 Tree segmentation

Our segmentation results were visually inspected to remove obvious errors. Manual corrections were required for 11 out of 118 trees, mainly due to over-segmentation of large trees (segments were merged) and under-segmentation of small trees adjacent to high objects (additional segments were created). The average overlap between the resulting polygons and their references totaled 91% with a standard deviation of 6% and a minimum value of 64.5%. A good match was obtained for more than half of our trees (Table 2). The spatial extent of tree canopies was more under- than over-estimated by our algorithm. For 16 out of 118 trees, not a single pure tree pixel could be identified during the subsequent canopy pixel selection procedure due to their small canopy size. These trees were removed from all further analyses.

Table 2: Classification of tree segmentation results based on fraction of overlapping area between reference polygons (ref) and segmentation results (result).

| | Overlap (reference perspective) $[A_{ref} - A_{(ref - result)}] / A_{ref}$ | Overlap (result perspective) $[A_{result} - A_{(result - ref)}] / A_{result}$ | Percentage of trees classified as... |
|----------------------------|---|--|--------------------------------------|
| 1 - Good match | > 90 % | > 90 % | 52 % |
| 2 - Low overestimation | > 90 % | < 90 % & > 75 % | 6 % |
| 3 - Low underestimation | < 90 % & > 75 % | > 90 % | 28 % |
| 4 - Medium overestimation | > 90 % | < 75 % & > 25 % | 1 % |
| 5 - Medium underestimation | < 75 % & > 25 % | > 90 % | 8 % |
| 6 - Severe overestimation | > 90 % | < 25 % | - |
| 7 - Severe underestimation | < 25 % | > 90 % | - |
| 8 - Low mismatch | < 90 % & > 75 % | < 90 % & > 75 % | 5 % |
| 9 - Medium mismatch | < 75 % & > 25 % | < 75 % & > 25 % | - |
| 10 - Severe mismatch | < 25 % | < 25 % | - |

A = area ; $x - y$ = shapefile generated by a difference operation using x as first input and y as second input.

4.2 Deriving chlorophyll content

PLSR outperformed both existing and locally calibrated spectral indices for deriving leaf chlorophyll content based on average canopy spectra (Table 3). Fifteen components were retained to run the global PLSR model, whereas seven components were used for the species-specific PLSR models (due to lower number of observations for individual species). Calibration performances (R^2 /RMSE) for the global model over 1000 iterations varied between 0.71/1.8 and 0.86/1.5 with average values of

0.78/1.7. Worse, best and average accuracy metrics for the subsequent validation stage amounted to 0.06/2.9, 0.89/1.2 and 0.48/2.1 respectively. Performance of the species-specific models was very similar compared to the global PLSR model, with average calibration and validation accuracies of 0.91/1.3 and 0.33/2.4 for *Acer*, 0.89/1.5 and 0.50/2.5 for *Aesculus*, 0.93/1.2 and 0.62/1.9 for *Platanus*, 0.77/1.7 and 0.42/2.4 for *Tilia*. The global PLSR model mainly relied on the red absorption feature (around 650 nm) and red edge feature (680 - 750 nm) to predict chlorophyll (Figure 8). Additionally, the model used more information from across the entire spectrum, with clear peaks at 1200 and 2250 nm. The same regions were found to be important for the species-specific PLSR models (not shown).

The normalized difference index generated using the OMNBR approach consisted of bands around 708 nm and 1666 nm and was the best performing chlorophyll index (Table 3). This approach was closely followed by a number of existing indices all making use of the red edge feature: MTCI, REP, mND705, ND705, SR705, Clrededge, Clgreen, NDRE, ZM and the Vogelmann red edge indices. GitGreen, GitRed, DDn, CARI, MCARI and NAOC showed weak correlations with chlorophyll, whereas SIPI, PRI, RGRI, PSRI, SR680, ND680, NDVI and 1DL_DGVI showed no correlation at all.

Table 3: Performance comparison of various spectral indices, PLSR and LiDAR-based approach for retrieving chlorophyll and Leaf Area Index from average tree canopy spectra (n = 102, except for LPM_{lasts} where n = 84). R² and RMSE values are reported for the linear fit between reference and estimated chlorophyll content / LAI. Results shown here represent the best results found along the pixel selection procedure (step 4 for chlorophyll and step 5 for LAI). More information on the effect of canopy pixel selection can be found in Section 4.4 and Supplement III.

| Abbreviation | Full name | Leaf or canopy level? | Source | R ² | RMS E |
|--------------------|---|-----------------------|-----------------------------|----------------|-------|
| CHLOROPHYLL | | | | | |
| VOG1 | Vogelmann red edge index 1 | Leaf | Vogelmann et al., 1993 | 0.41 | 7.9 |
| VOG2 | Vogelmann red edge index 2 | Leaf | Vogelmann et al., 1993 | 0.41 | 7.8 |
| VOG3 | Vogelmann red edge index 3 | Leaf | Vogelmann et al., 1993 | 0.41 | 7.9 |
| SIPI | Structure Insensitive Pigment Index | Leaf | Penuelas et al., 1995 | 0.04 | 29.5 |
| PRI | Photochemical Reflectance Index | Leaf | Gamon et al., 1997 | 0.18 | 13.7 |
| GitGreen | Gitelson Index Green | Leaf | Gitelson and Merzlyak, 1997 | 0.31 | 9.7 |
| GitRed | Gitelson Index Red | Leaf | Gitelson and Merzlyak, 1997 | 0.32 | 9.5 |
| RGRI | Red Green Ratio Index | Leaf | Gamon and Surfus, 1999 | 0.02 | 37.9 |
| PSRI | Plant Senescence Reflectance Index | Leaf | Merzlyak et al., 1999 | 0.01 | 47.8 |
| Clgreen | Chlorophyll Index Green | Leaf | Gitelson et al., 2003 | 0.40 | 8.0 |
| Clrededge | Chlorophyll Index Red Edge | Leaf | Gitelson et al., 2003 | 0.42 | 7.7 |
| SR680 | Simple Ratio 680 | Leaf | Sims and Gamon, 2002 | 0.06 | 23.6 |
| SR705 | Simple Ratio 705 | Leaf | Sims and Gamon, 2002 | 0.37 | 8.5 |
| mSR705 | Modified SR705 | Leaf | Sims and Gamon, 2002 | 0.40 | 8.1 |
| ND680 | Normalized Difference 680 | Leaf | Sims and Gamon, 2002 | 0.04 | 28.0 |
| ND705 | Normalized Difference 705 | Leaf | Sims and Gamon, 2002 | 0.37 | 8.4 |
| mND705 | Modified ND705 | Leaf | Sims and Gamon, 2002 | 0.43 | 7.5 |
| DDn | Double Deference Index | Leaf | Wang and Li, 2012 | 0.34 | 9.1 |
| NDVI | Normalized Difference Vegetation Index | Canopy | Rouse et al., 1973 | 0.04 | 29.2 |
| REP | Red Edge Position | Canopy | Horler et al., 1983 | 0.44 | 7.4 |
| 1DL_DGVI | First-order derivative green vegetation index with local baseline | Canopy | Elvidge and Chen, 1995 | 0.03 | 30.7 |
| NDRE | Normalized Difference Red Edge | Canopy | Barnes et al., 2000 | 0.41 | 7.9 |
| CARI | Chlorophyll Absorption in Reflectance Index | Canopy | Daughtry et al., 2000 | 0.31 | 9.7 |
| MCARI | Modified CARI | Canopy | Daughtry et al., 2000 | 0.31 | 9.7 |
| ZM | Zarco and Miller | Canopy | Zarco-Tejada et al., 2001 | 0.41 | 7.8 |
| MTCI | MERIS Terrestrial Chlorophyll Index | Canopy | Dash and Curran, 2004 | 0.46 | 7.1 |
| NAOC | Normalized Area Over Reflectance Curve | Canopy | Delegido et al., 2010 | 0.29 | 11.0 |
| OMNBR | Spectral index developed using the OMNBR approach | Canopy | This study | 0.46 | 7.0 |
| PLSR | Partial least squares model | Canopy | This study | 0.77 | 2.8 |
| PLSR_spp | Species-specific PLSR model | Canopy | This study | 0.83 | 2.4 |

Table 3 continued

| LEAF AREA INDEX | | | | | |
|----------------------|---|--------|-------------------------|------|-----|
| SR | Simple Ratio | Canopy | Jordan, 1969 | 0.10 | 3.1 |
| NDVI | Normalized Difference Vegetation Index | Canopy | Rouse et al., 1973 | 0.12 | 2.8 |
| SAVI | Soil Adjusted Vegetation Index | Canopy | Huete, 1988 | 0.25 | 1.8 |
| ARVI | Atmospherically Resistant Vegetation Index | Canopy | Kaufman and Tanré, 1992 | 0.11 | 3.0 |
| 1DL_DGVI | First-order derivative green vegetation index with local baseline | Canopy | Elvidge and Chen, 1995 | 0.27 | 1.8 |
| EVI | Enhanced Vegetation Index | Canopy | Huete et al., 1997 | 0.25 | 1.9 |
| VARI | Visible Atmospherically Resistant Index | Canopy | Gitelson et al., 2002 | 0.01 | 7.7 |
| Vigreen | Vegetation Index using Green Band | Canopy | Gitelson et al., 2002 | 0.01 | 8.3 |
| sLAIDI | Standardized LAI Determining Index | Canopy | Delalieux et al., 2008 | 0.27 | 1.8 |
| OMNBR | Spectral index developed using the OMNBR approach | Canopy | This study | 0.33 | 1.5 |
| PLSR | Partial least squares model | Canopy | This study | 0.66 | 0.5 |
| PLSR_spp | Species-specific PLSR model | Canopy | This study | 0.74 | 0.4 |
| LPM _{lasts} | Laser penetration metric from LiDAR | Canopy | Alonzo et al., 2015 | 0.56 | 0.4 |

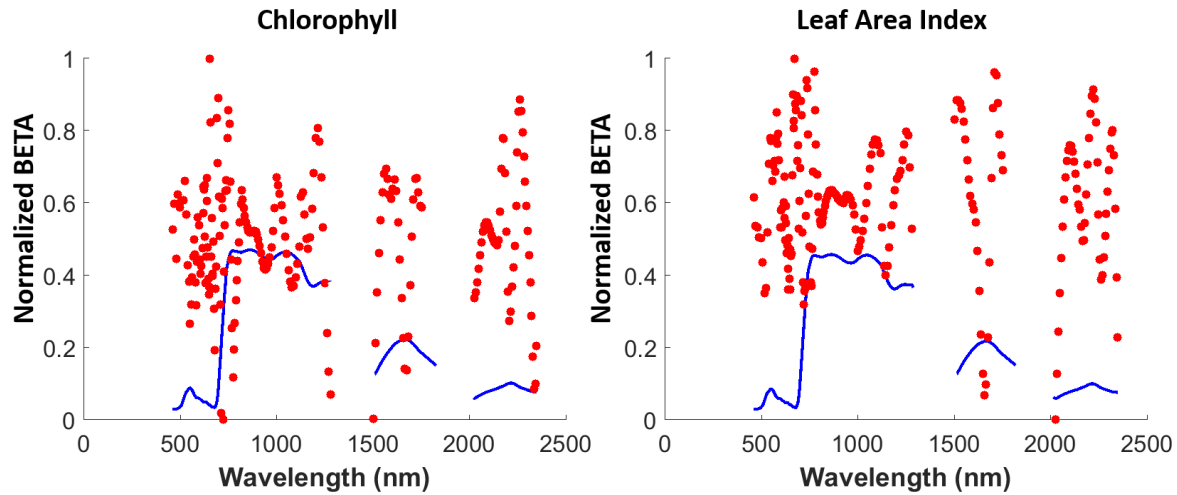


Figure 8: Contribution of each spectral band (expressed as normalized regression coefficient or beta; red dots) in the global PLSR model derived in this study to estimate chlorophyll content (left) and LAI (right) based on average canopy spectra. The blue line represents a typical tree canopy spectrum and enables easier interpretation of the results.

4.3 Deriving LAI

LAI of urban trees proved more difficult to derive from spectral data, with accuracies that were generally lower than those for chlorophyll (Table 3). LAI was best predicted using PLSR. Fifteen and seven components were used to build the global and species-specific PLSR models. Calibration of the global model resulted in model accuracies (R^2 /RMSE) between 0.56/0.76 and 0.77/0.67 with average values of 0.67/0.73. Subsequent validation yielded an average accuracy of 0.27/0.93 with a minimum of 0.01/1.25 and a maximum of 0.82/0.58. Species-specific PLSR models achieved similar but slightly better results, with average calibration and validation model accuracies of 0.87/0.66 and 0.27/1.37 for *Acer*, 0.82/0.68 and 0.25/1.14 for *Aesculus*, 0.70/0.60 and 0.21/0.93 for *Platanus* and 0.80/0.69 and 0.51/0.92 for *Tilia*. Compared to the chlorophyll model, more bands received high weights in the final PLSR model predicting LAI, including regions near the red absorption and red edge features, as well as large parts of the SWIR1 (1500 - 1750 nm) and SWIR2 (2000 - 2350 nm) regions (Figure 8). The NIR plateau (750 – 1250 nm) also contributed more to the LAI model than to the chlorophyll model.

Of all spectral indices tested, the OMNBR index (consisting of bands around 873 nm and 2240 nm) showed the lowest LAI prediction error. Similar accuracies were attained using different zones of the

spectrum, i.e. NIR region (sLAIDi), red region (1DL_DGVI) and combinations of NIR and red (EVI, SAVI). With R^2 values lower than 0.2, SR, NDVI, ARVI, VARI and Vlgreen failed to predict LAI. Laser penetration metrics derived from LiDAR data generally outperformed all spectral indices and approached the accuracies attained using PLSR.

4.4 Effect of pixel selection

The accuracy of chlorophyll content determination via spectral indices in general benefitted from extensive canopy pixel selection, except for the last step (Figure 9; detailed results in Supplement III). The magnitude of the effect however varied greatly between different spectral indices, with the least performing indices showing the highest gains in accuracy (NAOC, GitGreen, GitRed, DDn, ND705), whereas others (MTCI, REP) seemed not to be affected. PLSR was able to produce highly accurate results at every stage of the procedure. Spectral indices related to LAI also attained their highest accuracy after step 4 (OMNBR) or step 5 (all others). PLSR once again performed well at each step, which cannot be said for the other methods.

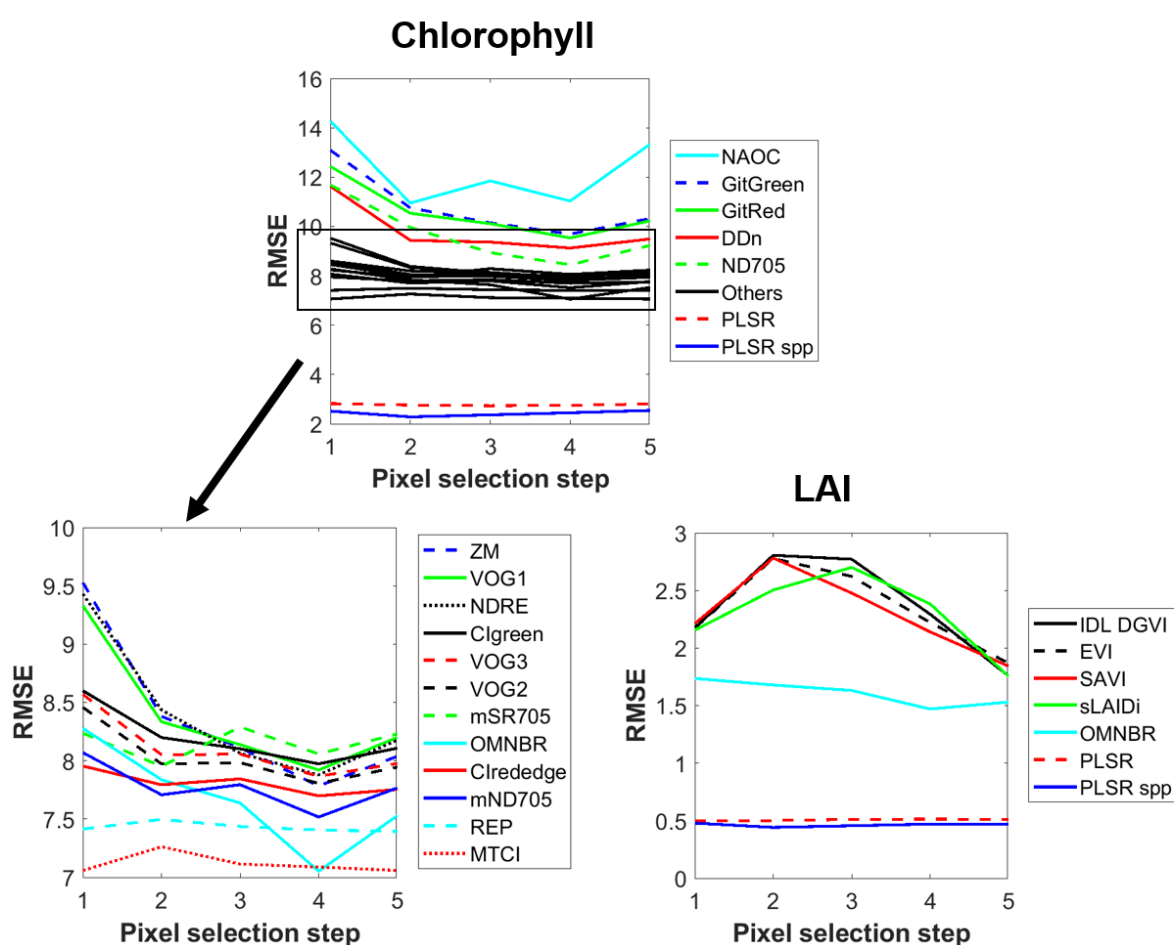


Figure 9: Comparison of accuracy (RMSE) for deriving chlorophyll content (left) and leaf area index (lower right) as a function of canopy pixel selection (1: no selection, 2: removal of edge pixels, 3: NDVI threshold, 4: grass index threshold, 5: brightness threshold). Methods showing no correlation with the variable of interest have been omitted from this figure. Detailed results for all methods can be consulted in Supplement III Supplement .

4.5 Sensitivity to remaining background signals

The sensitivity of chlorophyll estimation to the substrate beneath the canopy was found to be highly variable among methods (Figure 10). Existing spectral indices underestimated the chlorophyll content of low LAI trees located above impervious surfaces, whereas chlorophyll tended to be overestimated for trees above grass surfaces. This trend was found for all spectral indices tested, but was only

significant for NAOC (Figure 10), ZM, VOG1, VOG2, VOG3, DDn and NDRE. Methods involving model training based on local data (i.e. OMNBR and PLSR) on the other hand did not show this sensitivity (Figure 10). The same tests were also run for LAI, but no significant effect of background material could be found (not shown).

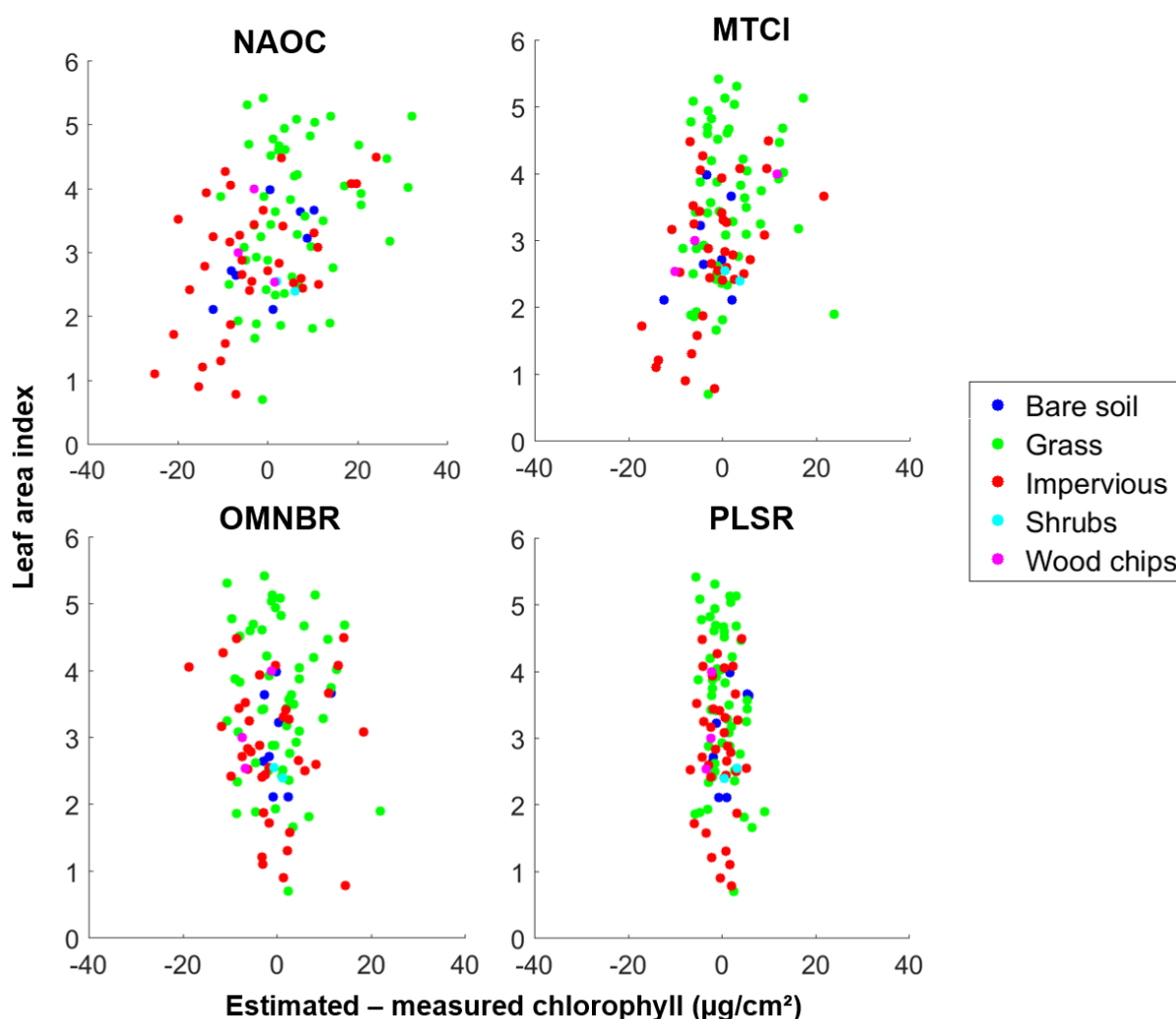


Figure 10: Difference between estimated and measured chlorophyll content of a tree in relation to its LAI and the material situated underneath the tree (indicated by colors). Negative values indicate underestimation of chlorophyll, whereas positive values imply overestimation. Results are only shown for four methods used to estimate chlorophyll content.

Many indices resulted in chlorophyll values close to or just below zero when applied on pure spectra of background materials (Table 4), particularly the NAOC index. Our PLSR model, CARI and MCARI however consistently predicted chlorophyll values for background materials that one would expect for (unhealthy) vegetation. Results for OMNBR, MTCI and REP were inconsistent, containing both large positive and negative values. Hence, the presence of these background signals in tree spectra can potentially have a major impact on the chlorophyll value extracted using these methods. Results for LAI show more reasonable values. Except for the PLSR model, all indices tested result in clear negative LAI values for non-vegetated surfaces.

Table 4: Predicted chlorophyll concentration and Leaf Area Index of different background materials. Results are presented as 'average' ['minimum', 'maximum']. Results deviating greatly from zero or approaching values typically found for vegetation are marked in bold. Methods consistently showing such values are also marked in bold.

| | Asphalt (n = 24) | Concrete (n = 38) | Soil (n = 19) | Water (n = 21) |
|------------------------|--------------------------------|----------------------------|----------------------------|-------------------------------|
| CHLOROPHYLL | | | | |
| GitGreen | -5.3 [-6.4,-3.7] | -5.0 [-6.4,-3.5] | -0.5 [-5.1, 7.8] | -8.9 [-14.4,17.7] |
| GitRed | -1.1 [-1.6, 0.4] | -1.0 [-1.6,-0.1] | 0.1 [-1.1, 4.0] | -5.0 [-9.4,10.5] |
| Clgreen | 8.8 [7.0,14.6] | 7.9 [5.8,11.1] | 10.5 [7.2,18.0] | 2.8 [-3.2,21.0] |
| Clrededge | -4.7 [-9.3, 5.5] | -5.5 [-11.8, 6.3] | -4.5 [-8.5, 5.7] | -29.0 [-856.4,320.8] |
| ZM | -0.9 [-1.9, 1.5] | -0.8 [-1.9, 0.5] | 0.8 [-1.2, 6.2] | -11.6 [-20.3, 4.8] |
| VOG1 | -6.5 [-8.1,-2.7] | -5.9 [-7.6,-4.2] | -3.9 [-6.8, 4.0] | -32.9 [-54.6,-5.0] |
| VOG2 | 2.3 [0.2, 4.5] | 2.5 [0.6, 5.1] | 4.4 [1.6,10.5] | -5.2 [-17.0, 3.2] |
| VOG3 | 4.3 [2.6, 6.1] | 4.4 [2.9, 6.4] | 6.0 [3.7,11.1] | -1.3 [-8.9, 5.1] |
| DDn | 7.6 [4.4,10.0] | 3.2 [-3.2,13.6] | -0.6 [-13.5,13.8] | 4.6 [-15.9,10.8] |
| mND705 | -32.4 [-44.4,-9.3] | -33.3 [-43.8,-15.6] | -31.0 [-39.1,-10.6] | -8.2 [-1130.8,719.7] |
| ND705 | -37.5 [-40.8,-29.4] | -36.9 [-40.7,-32.2] | -31.3 [-38.0,-14.5] | -84.0 [-138.9,-2.8] |
| SR705 | -0.6 [-1.3, 1.1] | -0.5 [-1.2, 0.5] | 0.8 [-0.7, 5.0] | -6.5 [-11.8, 8.9] |
| mSR705 | 4.7 [2.9, 9.2] | 4.5 [2.9, 7.7] | 4.9 [3.6, 8.9] | -32.6 [-400.8,50.9] |
| REP | 252.4 [32.0,3905.2] | 41.4 [0.8,176.7] | 23.6 [-30.5,59.2] | 145.5 [-14.0,1553.7] |
| NAOC | 0.2 [0.1, 0.4] | 0.2 [0.1, 0.4] | 0.7 [0.1, 2.7] | 12.4 [1.1,38.3] |
| CARI | 68.6 [65.7,69.8] | 69.3 [62.9,73.9] | 63.1 [38.6,74.6] | 57.1 [31.2,68.7] |
| MCARI | 72.0 [68.6,73.5] | 73.0 [65.5,78.4] | 66.9 [40.9,79.6] | 59.8 [32.2,72.6] |
| MTCI | -228.4 [-4919.0,1022.0] | 17.5 [-250.6,214.8] | 28.2 [7.1,55.4] | -282.9 [-7440.3,848.4] |
| NDRE | -15.7 [-18.8,-9.2] | -15.4 [-20.7,-9.9] | -10.2 [-16.4, 3.3] | -57.2 [-112.2,-6.2] |
| OMNBR | -9.7 [-22.5, 0.5] | -3.3 [-29.1,39.8] | -15.8 [-35.3,16.6] | 62.3 [29.9,98.0] |
| PLSR | 31.2 [26.9,36.5] | 26.9 [14.3,39.7] | 14.4 [-3.0,30.5] | 22.3 [6.6,27.9] |
| LEAF AREA INDEX | | | | |
| 1DL_DGVI | -5.4 [-5.9,-4.9] | -5.4 [-6.2,-4.4] | -4.8 [-5.9,-2.3] | -5.3 [-6.1,-2.5] |
| EVI | -9.1 [-9.6,-8.3] | -9.0 [-10.5,-7.6] | -7.5 [-9.2,-4.1] | -9.7 [-11.1,-6.1] |
| SAVI | -11.2 [-11.7,-10.1] | -11.1 [-12.7,-9.2] | -8.8 [-11.3,-4.0] | -11.9 [-13.8,-6.9] |
| sLAIDI | -6.1 [-8.3,-4.0] | -4.4 [-10.1, 1.8] | -6.9 [-13.9, 1.3] | -6.5 [-7.8,-3.6] |
| OMNBR | -12.5 [-14.5,-10.5] | -14.6 [-25.7,-10.5] | -13.7 [-21.8,-7.5] | -13.4 [-34.4,-1.0] |
| PLSR | 1.4 [-0.5, 3.5] | 3.5 [-4.5, 8.9] | 3.1 [-5.3, 9.6] | 3.0 [-0.0, 4.0] |

4.6 Integrated urban tree health indicator

We selected the global (non-species specific) PLSR model to compute a final chlorophyll and LAI value for each tree in our dataset. Based on these, we derived a final defoliation, discoloration and tree damage score (0-3) and directly compared this outcome to the same scores obtained through a purely visual assessment (Section 2.3.4) using a confusion matrix approach (Table 5). Agreement between the remote sensing based and the visual analysis was slightly lower for discoloration compared to defoliation. For about 60% of the trees, the scores provided by the two methods matched perfectly. A strong disagreement between the methods (> 1 class) only occurred for 6% of the trees. In general, the remote sensing based method was more conservative regarding tree health compared to the visual analysis, i.e. the chance of a tree being labeled as unhealthy was lower. This observation was more pronounced for discoloration compared to defoliation. As a result, accuracies for the healthy class (0) were higher compared to the unhealthy classes. If trees having scores of 0 or 1 were considered healthy, the chance for a visually healthy tree being labeled as healthy using our method was 93%. Visually unhealthy trees had a chance of 71% of being identified as unhealthy. Detailed accuracy reports per tree species are included in Supplement IV, but did not deviate significantly from the overall results presented in Table 5.

Table 5: Accuracy metrics derived from the confusion matrices comparing defoliation, discoloration and tree damage scores between visually based and remote sensing based assessment. PA = producer accuracy. UA = user accuracy. “n Δ class = x” = number of trees for which the variable at hand is over- or underestimated by x classes. “n RS > visual” = number of trees for which the score is larger for the remote sensing approach compared to the visual approach, meaning tree health is underestimated.

| Metric | Defoliation | Discoloration | Damage |
|---------------------|-------------|---------------|-------------|
| Total accuracy | 0.62 | 0.60 | 0.62 |
| Kappa | 0.46 | 0.38 | 0.48 |
| PA / UA class 0 | 0.73 / 0.79 | 0.79 / 0.73 | 0.75 / 0.83 |
| PA / UA class 1 | 0.62 / 0.47 | 0.47 / 0.42 | 0.71 / 0.45 |
| PA / UA class 2 | 0.61 / 0.52 | 0.59 / 0.56 | 0.33 / 0.35 |
| PA / UA class 3 | 0.25 / 1 | 0 / - | 0.52 / 0.75 |
| PA / UA class 0 + 1 | 0.91 / 0.85 | 0.94 / 0.86 | 0.93 / 0.83 |
| PA / UA class 2 + 3 | 0.69 / 0.8 | 0.52 / 0.72 | 0.71 / 0.88 |
| n Δ class = 0 | 63 | 61 | 63 |
| n Δ class = 1 | 33 | 35 | 32 |
| n Δ class = 2 | 6 | 4 | 6 |
| n Δ class = 3 | 0 | 2 | 1 |
| n RS > visual | 16 | 14 | 17 |
| n RS < visual | 23 | 27 | 22 |

5 Discussion

5.1 Tree segmentation

Compared to forests, cities host a large diversity of trees with respect to species, size, shape and local context. Defining one set of criteria that enables perfect delineation of such a diverse set of urban trees proved to be challenging. Using a relatively simple classification and segmentation algorithm, we generated segmentation results of acceptable quality that, given some minor manual corrections, could easily be fed into the remainder of our tree health workflow. Recently, many advanced tree segmentation techniques have been proposed (Zhao et al., 2017; Zhen et al., 2016), which could be used to improve our results even further. One specific suggestion would be to locate individual tree stems using the LiDAR data, which could then be used as an additional constraint in the canopy segmentation process (Reitberger et al., 2009). This was however beyond the scope of this paper. We tended to underestimate actual tree extents, but given the particular purpose of tree segmentation in this study (i.e. defining regions for extracting spectral information), we believe this bias did not affect further analyses as it merely caused (contaminated) tree edges to be excluded.

5.2 Tree property retrieval

In general, approaches which require local calibration (PLSR, OMNBR) were found to perform better compared to existing spectral indices for deriving tree properties from average canopy spectra (Table 3). An important prerequisite for using these techniques is the availability of an extensive local calibration dataset. Ideally, this dataset contains all species occurring within the study area, allowing the construction of species-specific PLSR models, as these performed best. Based on our results in Table 3 however, pooling similar species together in one generic model represents an acceptable alternative. Given the large variation we observed in the PLSR model calibration and validation accuracies, we conclude PLSR to be highly sensitive to the specific calibration data fed into the model. Although not specifically tested, this leads us to believe that the portability of our models generated for broadleaf tree species in Brussels to other tree species and cities is rather limited. The strength of data fitting approaches such as PLSR is its reduced sensitivity to data artefacts introduced due to the specific conditions at the time of data acquisition (e.g. sensor used, atmosphere, sun-sensor geometry, pre-processing). This adds to their reduced portability, as opposed to existing spectral indices which generally have a solid physical basis and in theory should be more widely applicable. Therefore, the

PLSR models created here should not be blindly applied to different regions, species and sensors not included in the present study without additional collection of local calibration data. The construction of more transferable, or generalizable, PLSR models for the prediction of urban tree chlorophyll and LAI would require the use of multiple datasets from various sources during the model calibration stage, as was illustrated by Martin et al. (2008) for forest nitrogen content, but was beyond the scope of this paper.

A second reason why PLSR significantly outperformed spectral indices lays in the number of bands used. Unlike spectral indices, PLSR makes use of the entire wealth of information contained in the spectra (Figure 8) to account for additional confounding factors such as differing backgrounds. Using a relatively simple pixel selection procedure, we were able to remove some of these background effects (Figure 9), but definitely not all (Figure 10). For instance, distinction between grass and tree spectra is known to be challenging due to high spectral similarity (e.g. Degerickx et al., 2017a). Our grass index relied on the NIR region (Figure 6), known to be correlated with the 3D arrangement of individual leaves (especially the 1050 nm band; Delalieux et al., 2008), and therefore did a reasonable but not perfect job of separating the two. Complete elimination of background signals from tree spectra would ideally require advanced ray-tracing techniques (Somers et al., 2014; Stuckens et al., 2009), which are typically computationally and data intensive and hence not suitable to be applied at the city scale. Alternatively, signal unmixing (Somers et al., 2009b; Tits et al., 2013, 2012) could be used, which theoretically allows for the reconstruction of the spectra of the pure materials within a mixed pixel. Although successfully applied in homogeneous plantations (Tits et al., 2014), this method would need some adaptations as some of its key assumptions (i.e. uniformity of background) are not valid in complex urban scenes. Instead of attempting to completely eliminate all background contamination, we would rather opt for an approach like PLSR which is able to cope with this interference (Figure 10; Supplement III).

In absence of local calibration data, this study suggests which spectral indices should (and should not) be used to derive chlorophyll content and LAI from urban trees (Table 3). In general, indices specifically incorporating the red edge feature all performed equally well and are to be recommended for chlorophyll prediction, irrespective whether designed for leaf spectra (CIGreen, CIRededge, VOG1-3, mSR705, mND705) or canopy spectra (MTCI, NDRE, ZM, REP). Notable exceptions are the PSRI and NAOC indices, which yielded significantly lower accuracies. PSRI was specifically created to detect the onset of leaf senescence (Merzlyak et al., 1999), whereas NAOC likely incorporates too many irrelevant bands (Delegido et al., 2010). CIgreen and CIRededge (Gitelson et al., 2003) outperformed the related indices GitGreen and GitRed (Gitelson and Merzlyak, 1997), confirming the recommendation from the former authors of using broad spectral regions instead of narrow bands for calculating chlorophyll indices to reduce sensitivity to leaf thickness. The well-known relation between the red edge feature and chlorophyll content, and its low sensitivity to ground cover, biomass and background (Horler et al., 1983; Vogelmann et al., 1993), were additionally confirmed by its presence in the OMNBR chlorophyll index and its dominance in the PLSR model for chlorophyll (Figure 8).

No clear relationship existed between the performance of a chlorophyll index (Table 3) and its sensitivity to background materials (Table 4). The NAOC index was found to be least sensitive to non-vegetation materials, but performed poorly compared to the highly sensitive MTCI and REP. CARI and MCARI, on the other hand, showed chlorophyll values for impervious surfaces one would expect for healthy vegetation, potentially explaining their poor performance. As discussed above, the removal of all background artefacts from urban tree spectra is considered a complex challenge, therefore we would recommend avoiding the use of spectral indices showing a high sensitivity, despite their reasonable performances here. The fact that OMNBR and especially PLSR showed high sensitivity was

caused by the fact that these signals were not completely removed from our tree spectra using pixel selection (Figure 10) and hence were partly used as training information during the construction of a chlorophyll index/PLSR model.

Identifying the most prominent spectral region to derive LAI was less straightforward, as multiple regions contributed equally well to this property (most notably the red edge and SWIR1 regions, Figure 8). Out of all indices tested, sLAIDi was found to perform best. This index, originally produced for fruit orchards, combines specific bands in the NIR and SWIR1 regions which were found to be insensitive to species and various stress factors at the leaf level (Delalieux et al., 2008; in turn explaining the significance of these spectral zones in the PLSR results). The additional correction for water content lead to an index solely sensitive to LAI. Still, accuracies for LAI retrieval based on spectral data were significantly lower than those for chlorophyll (Table 3). Our test using laser penetration metrics has however clearly shown the potential of LiDAR data in this respect. Given that this approach yielded similar accuracies compared to PLSR, has a solid physical basis and hence does not suffer from potential transferability issues discussed above, we would recommend using LiDAR data instead of hyperspectral data for deriving LAI from urban trees in future work.

5.3 Potential applications of our tree health workflow

Application of the proposed urban tree health workflow at the city scale would generate spatially extensive tree maps showing defoliation, discoloration and an integrated tree damage indicator, all closely related to a traditional visual assessment (Table 5). As visual leaf color is not solely driven by chlorophyll concentration, but affected by many more leaf pigments (e.g. anthocyanin, carotenes), the match for discoloration between the two suites of methods was found to be lower compared to defoliation. An important difference to note is that defoliation and discoloration derived from remote sensing data are continuous variables and can therefore provide more detail and nuance as opposed to the ordinal scores retrieved from visual analysis. Moreover, if applied at the pixel level instead of the canopy level (as was done here), these data could provide additional insight in the spatial variation of tree health within individual canopies. Given that imagery is collected (bi-) annually at the peak of the vegetation season, our products can provide a detailed indication of urban tree health status and possible underlying causes at the city-wide scale and could form a solid basis of a long term urban tree health monitoring program. The traditional VTA approach however includes other aspects of tree health that are hard to assess using airborne remote sensing data (e.g. root damage, soil compaction, trunk deformation, stability, identification of pests and diseases). We therefore would argue for an integration of both approaches (as also suggested by Lawley et al. (2016) for monitoring of natural vegetation), where remote sensing is used to identify problematic areas with regard to tree health, thus allowing urban green managers to set their management and monitoring priorities in a more efficient way. The produced tree health maps also provide a valuable tool for further scientific research. By correlating our maps with spatial information on e.g. imperviousness (Plowright et al., 2017), air pollution or traffic intensity (Delegido et al., 2014), the dominant drivers of urban tree health could be assessed, in turn contributing to a better understanding of tree functioning in urban environments.

Aside from the final tree health map, our intermediate results also represent valuable products. Delineated tree segments provide a city wide estimation of tree coverage and can serve as a basis for deriving various other tree properties, either directly (e.g. tree dimensions) or indirectly using additional data sources (e.g. hyperspectral or thermal data). Maps of chlorophyll content and LAI can additionally be used as inputs to conduct a spatially-explicit assessment of ecosystem services provided by urban trees. In particular, LAI is frequently used in ecosystem service models (e.g. iTree Eco) as it is

linked to a tree's capacity to intercept water (Xiao et al., 2000), filter air pollution (Nowak et al., 1998) and mitigate extreme temperatures (Lin and Lin, 2010).

5.4 Further recommendations

This study was limited to two tree properties, chlorophyll content and LAI, for tree health prediction, since our goal was to develop a remote sensing based alternative for the established VTA approach. Since hyperspectral data contain a wealth of information with regard to plant properties such as water content (Clevers et al., 2010) and nitrogen content (Townsend et al., 2003), our approach could be extended to account for additional aspects of tree health, particularly water and nutrient stress. Due to the large array of natural defense mechanisms of trees to respond to stress (Günthardt-Goerg and Vollenweider, 2007), there can be significant time lags between the onset of a particular stress factor and the moment when a tree becomes visually unhealthy. Solely relying on defoliation and discoloration could therefore decrease the chance that any remediation attempt could be undertaken by urban green managers, or that those attempts would be successful. Our approach should therefore be complemented with methods allowing early detection of tree stress. Regular and detailed quantification of additional plant pigments, like anthocyanin and carotenes (both linked to tree stress; Gitelson et al., 2009; Gitelson et al., 2002), using hyperspectral data could be a valuable strategy. Various other approaches based on hyperspectral, thermal and/or fluorescence data, have already shown their potential in this respect (Carter et al., 1996; Chaerle and Van Der Straeten, 2000; López-López et al., 2016). More research is needed to test these approaches in the complex urban environment.

6 Conclusion

In this paper we proposed a workflow to derive urban tree health information based on airborne remote sensing data. After delineating each individual tree using airborne LiDAR data, we successfully created local PLSR models to retrieve both chlorophyll content and LAI from hyperspectral data. Existing spectral indices showed lower accuracies due to contamination of the tree spectra by background materials, but are believed to be better transferable to other cities, sensors and species compared to PLSR. Laser penetration metrics derived from LiDAR constitute a decent alternative to PLSR for LAI retrieval. By comparing chlorophyll content and LAI with species-specific reference values, we were able to accurately retrieve information on discoloration and defoliation respectively, yielding similar results as the traditional visual tree health assessment. Although our approach would by no means eliminate the need for visual assessment, constructing spatially explicit maps of discoloration and defoliation on an annual basis at the city scale would provide an excellent tool for urban green managers, allowing them to set monitoring priorities and manage the valuable natural capital of our cities in a more efficient way. Future research efforts should be devoted to early detection methods of tree stress in urban areas.

7 Acknowledgements

The research presented in this paper is funded by the Belgian Science Policy Office in the framework of the STEREOIII program (UrbanEARS project (SR/00/307) and BelAir project (SR/01/354) for acquisition of hyperspectral data of Brussels). In addition, the authors would like to thank dr. Mike Alonzo for his guidance on the use of LiDAR data and his valuable suggestions. Special thanks also to prof. Frieke Van Coillie and Susan Meerdink for their guidance on respectively the tree segmentation algorithm and Partial Least Squares regression. We would like to acknowledge all institutions and their staff which kindly provided us with valuable datasets contributing to this work: Max Fontaine from the Green Management Office of the City of Brussels for providing tree species data for the city of Brussels, Sébastien De France from the Brussels Regional Information Centre for the 2012 LiDAR dataset and

635 Matthias Engelbeen from Brussels Environment for providing us insights in the needs of urban green
636 managers.

637 8 References

- 638 Alonzo, M., Bookhagen, B., McFadden, J.P., Sun, A., Roberts, D.A., 2015. Mapping urban forest leaf
639 area index with airborne lidar using penetration metrics and allometry. *Remote Sens. Environ.*
640 162, 141–153. <https://doi.org/10.1016/j.rse.2015.02.025>
- 641 Alonzo, M., Bookhagen, B., Roberts, D.A., 2014. Urban tree species mapping using hyperspectral and
642 lidar data fusion. *Remote Sens. Environ.* 148, 70–83. <https://doi.org/10.1016/J.Rse.2014.03.018>
- 644 Asner, G.P., Martin, R.E., Knapp, D.E., Tupayachi, R., Anderson, C., Carranza, L., Martinez, P.,
645 Houcheime, M., Sinca, F., Weiss, P., 2011. Spectroscopy of canopy chemicals in humid tropical
646 forests. *Remote Sens. Environ.* 115, 3587–3598. <https://doi.org/10.1016/j.rse.2011.08.020>
- 647 Barnes, E.M., Clarke, T.R., Richards, S.E., Colaizzi, P.D., Haberl, J., Kostrzewski, M., Waller, P., Choi, C.,
648 Riley, E., Thompson, T., Lascano, R.J., Li, H., Moran, M.S., 2000. Coincident Detection of Crop
649 Water Stress, Nitrogen Status and Canopy Density Using Ground Based Multispectral Data.
650 *Proc. FIFTH Int. Conf. Precis. Agric.*
- 651 Berk, A., Anderson, G.P., Bernstein, L.S., Acharya, P.K., Dothe, H., Matthew, M.W., Adler-Golden,
652 S.M., Chetwynd, Jr., J.H., Richtsmeier, S.C., Pukall, B., Allred, C.L., Jeong, L.S., Hoke, M.L., 1999.
653 MODTRAN4 radiative transfer modeling for atmospheric correction, in: Larar, A.M. (Ed.), .
654 *International Society for Optics and Photonics*, p. 348. <https://doi.org/10.1117/12.366388>
- 655 Berrang, P., Karnosky, D.F., Stanton, B.J., 1985. Environmental factors affecting tree health in New
656 York City. *J. Arboric.* 11, 185–189.
- 657 Biesemans, J., Sterckx, S., Knaeps, E., Vreys, K., Adriaensen, S., Hooy, J., 2007. Image Processing
658 Workflows for Airborne Remote. *Proc. 5th EARSeL Work. Imaging Spectrosc.* 1–14.
659 <https://doi.org/10.1007/b139115>
- 660 Bolund, P., Hunhammar, S., 1999. Ecosystem services in urban areas. *Ecol. Econ.* 29, 293–301.
661 [https://doi.org/10.1016/S0921-8009\(99\)00013-0](https://doi.org/10.1016/S0921-8009(99)00013-0)
- 662 Carter, G.A., Cibula, W.G., Miller, R.L., 1996. Narrow-band reflectance imagery compared with
663 thermal imagery for early detection of plant stress. *J. Plant Physiol.* 148, 515–522.
664 [https://doi.org/10.1016/S0176-1617\(96\)80070-8](https://doi.org/10.1016/S0176-1617(96)80070-8)
- 665 Chaerle, L., Van Der Straeten, D., 2000. Imaging techniques and the early detection of plant stress.
666 *Trends Plant Sci.* 5, 495–501. [https://doi.org/10.1016/S1360-1385\(00\)01781-7](https://doi.org/10.1016/S1360-1385(00)01781-7)
- 667 Clevers, J.G.P.W., Kooistra, L., Schaepman, M.E., 2010. Estimating canopy water content using
668 hyperspectral remote sensing data. *Int. J. Appl. Earth Obs. Geoinf.* 12, 119–125.
669 <https://doi.org/10.1016/J.JAG.2010.01.007>
- 670 Cregg, B., Dix, M.E., 2001. Tree moisture stress and insect damage in urban areas in relation to heat
671 island effects. *J. Arboric.* 27, 8–17.
- 672 Czerniawska-Kusza, I., Kusza, G., Dużyński, M., 2004. Effect of deicing salts on urban soils and health
673 status of roadside trees in the Opole Region. *Environ. Toxicol.* 19, 296–301.
674 <https://doi.org/10.1002/tox.20037>
- 675 Dash, J., Curran, P.J., 2004. The MERIS terrestrial chlorophyll index. *Int. J. Remote Sens.* 25, 5403–
676 5413. <https://doi.org/10.1080/0143116042000274015>

677 Daughtry, C.S.T., Walthall, C.L., Kim, M.S., de Colstoun, E.B., McMurtrey, J.E., 2000. Estimating corn
678 leaf chlorophyll concentration from leaf and canopy reflectance. *Remote Sens. Environ.* 74,
679 229–239. [https://doi.org/10.1016/S0034-4257\(00\)00113-9](https://doi.org/10.1016/S0034-4257(00)00113-9)

680 Day, S.D., Bassuk, N.L., 1994. A review of the effects of soil compaction and amelioration techniques
681 on landscape trees. *J. Arboric.* 20, 9–17. <https://doi.org/10.1080/03071375.2009.9747583>

682 Degerickx, J., Hermy, M., Somers, B., 2017a. Mapping functional urban green types using
683 hyperspectral remote sensing, in: 2017 Joint Urban Remote Sensing Event, JURSE 2017.
684 <https://doi.org/10.1109/JURSE.2017.7924553>

685 Degerickx, J., Okujeni, A., Iordache, M.-D., Hermy, M., van der Linden, S., Somers, B., 2017b. A novel
686 spectral library pruning technique for spectral unmixing of Urban land cover. *Remote Sens.* 9.
687 <https://doi.org/10.3390/rs9060565>

688 Delalieux, S., Somers, B., Hereijgers, S., Verstraeten, W.W., Keulemans, W., Coppin, P., 2008. A near-
689 infrared narrow-waveband ratio to determine Leaf Area Index in orchards. *Remote Sens.*
690 *Environ.* 112, 3762–3772. <https://doi.org/10.1016/j.rse.2008.05.003>

691 Delegido, J., Alonso, L., González, G., Moreno, J., 2010. Estimating chlorophyll content of crops from
692 hyperspectral data using a normalized area over reflectance curve (NAOC). *Int. J. Appl. Earth*
693 *Obs. Geoinf.* 12, 165–174. <https://doi.org/10.1016/j.jag.2010.02.003>

694 Delegido, J., Van Wittenberghe, S., Verrelst, J., Ortiz, V., Veroustraete, F., Valcke, R., Samson, R.,
695 Rivera, J.P., Tenjo, C., Moreno, J., 2014. Chlorophyll content mapping of urban vegetation in the
696 city of Valencia based on the hyperspectral NAOC index. *Ecol. Indic.* 40, 34–42.
697 <https://doi.org/10.1016/j.ecolind.2014.01.002>

698 Elvidge, C.D., Chen, Z., 1995. Comparison of broad-band and narrow-band red and near-infrared
699 vegetation indices. *Remote Sens. Environ.* 54, 38–48. [https://doi.org/10.1016/0034-](https://doi.org/10.1016/0034-4257(95)00132-K)
700 [4257\(95\)00132-K](https://doi.org/10.1016/0034-4257(95)00132-K)

701 Fink, S., 2009. Hazard tree identification by visual tree assessment (VTA): scientifically solid and
702 practically approved. *Arboric. J.* 32, 139–155.

703 Gamon, J.A., Serrano, L., Surfus, J.S., 1997. The photochemical reflectance index: An optical indicator
704 of photosynthetic radiation use efficiency across species, functional types, and nutrient levels.
705 *Oecologia* 112, 492–501. <https://doi.org/10.1007/s004420050337>

706 Gamon, J.A., Surfus, J.S., 1999. Assessing leaf pigment content and activity with a reflectometer. *New*
707 *Phytol.* 143, 105–117. <https://doi.org/10.1046/j.1469-8137.1999.00424.x>

708 Gitelson, A.A., Chivkunova, O.B., Merzlyak, M.N., 2009. Nondestructive estimation of anthocyanins
709 and chlorophylls in anthocyanic leaves. *Am. J. Bot.* 96, 1861–1868.
710 <https://doi.org/10.3732/ajb.0800395>

711 Gitelson, A.A., Gritz, Y., Merzlyak, M.N., 2003. Relationships between leaf chlorophyll content and
712 spectral reflectance and algorithms for non-destructive chlorophyll assessment in higher plant
713 leaves. *J. Plant Physiol.* 160, 271–82. <https://doi.org/10.1078/0176-1617-00887>

714 Gitelson, A.A., Kaufman, Y.J., Stark, R., Rundquist, D., 2002. Novel algorithms for remote estimation
715 of vegetation fraction. *Remote Sens. Environ.* 80, 76–87. [https://doi.org/10.1016/S0034-](https://doi.org/10.1016/S0034-4257(01)00289-9)
716 [4257\(01\)00289-9](https://doi.org/10.1016/S0034-4257(01)00289-9)

717 Gitelson, A.A., Merzlyak, M.N., 1997. Remote estimation of chlorophyll content in higher plant
718 leaves. *Int. J. Remote Sens.* 18, 2691–2697. <https://doi.org/10.1080/014311697217558>

719 Gitelson, A.A., Zur, Y., Chivkunova, O.B., Merzlyak, M.N., 2002. Assessing carotenoid content in plant

720 leaves with reflectance spectroscopy. *Photochem. Photobiol.* 75, 272–281.
721 [https://doi.org/10.1562/0031-8655\(2002\)0750272ACCIPL2.O.CO2](https://doi.org/10.1562/0031-8655(2002)0750272ACCIPL2.O.CO2)

722 Günthardt-Goerg, M.S., Vollenweider, P., 2007. Linking stress with macroscopic and microscopic leaf
723 response in trees: New diagnostic perspectives. *Environ. Pollut.* 147, 467–488.
724 <https://doi.org/10.1016/j.envpol.2006.08.033>

725 Heiden, U., Segl, K., Roessner, S., Kaufmann, H., 2007. Determination of robust spectral features for
726 identification of urban surface materials in hyperspectral remote sensing data. *Remote Sens.*
727 *Environ.* 111, 537–552. <https://doi.org/10.1016/j.rse.2007.04.008>

728 Helland, I., Helland, Inge, 2006. Partial Least Squares Regression, in: *Encyclopedia of Statistical*
729 *Sciences*. John Wiley & Sons, Inc., Hoboken, NJ, USA.
730 <https://doi.org/10.1002/0471667196.ess6004.pub2>

731 Horler, D.N.H., Dockray, M., Barber, J., 1983. The red edge of plant leaf reflectance. *Int. J. Remote*
732 *Sens.* 4, 273–288. <https://doi.org/10.1080/01431168308948546>

733 Huete, A.R., 1988. A soil-adjusted vegetation index (SAVI). *Remote Sens. Environ.* 25, 295–309.
734 [https://doi.org/10.1016/0034-4257\(88\)90106-X](https://doi.org/10.1016/0034-4257(88)90106-X)

735 Huete, A.R., Liu, H.Q., Batchily, K., J., L. van W., 1997. A comparison of vegetation indices over a
736 Global set of TM images for EO -MODIS. *Remote Sens. Environ.* 59, 440–451.

737 Jordan, C.F., 1969. Derivation of Leaf-Area Index from Quality of Light on the Forest Floor. *Ecology*
738 50, 663–666. <https://doi.org/10.2307/1936256>

739 Kaufman, Y.J., Tanré, D., 1992. Atmospherically Resistant Vegetation Index (ARVI) for EOS-MODIS.
740 *IEEE Trans. Geosci. Remote Sens.* 30, 261–270. <https://doi.org/10.1109/36.134076>

741 Klingberg, J., Konarska, J., Lindberg, F., Johansson, L., Thorsson, S., 2017. Mapping leaf area of urban
742 greenery using aerial LiDAR and ground-based measurements in Gothenburg, Sweden. *Urban*
743 *For. Urban Green.* 26, 31–40. <https://doi.org/10.1016/j.ufug.2017.05.011>

744 Lakatos, F., Mirtchev, S., Mehmeti, A., Shabanaj, H., 2014. Manual for visual assessment of forest
745 crown condition. Rome, Italy.

746 Lawley, V., Lewis, M., Clarke, K., Ostendorf, B., 2016. Site-based and remote sensing methods for
747 monitoring indicators of vegetation condition: An Australian review. *Ecol. Indic.* 60, 1273–1283.
748 <https://doi.org/10.1016/j.ecolind.2015.03.021>

749 Lichtenthaler, H.K., 1987. [34] Chlorophylls and carotenoids: Pigments of photosynthetic
750 biomembranes. *Methods Enzymol.* 148, 350–382. [https://doi.org/10.1016/0076-](https://doi.org/10.1016/0076-6879(87)48036-1)
751 [6879\(87\)48036-1](https://doi.org/10.1016/0076-6879(87)48036-1)

752 Lin, B.S., Lin, Y.J., 2010. Cooling effect of shade trees with different characteristics in a subtropical
753 urban park. *HortScience* 45, 83–86.

754 Lonsdale, D., 1999. Principles of tree hazard assessment and management. Stationery Office Ltd,
755 Publications Centre, London.

756 López-López, M., Calderón, R., González-Dugo, V., Zarco-Tejada, P.J., Fereres, E., 2016. Early
757 detection and quantification of almond red leaf blotch using high-resolution hyperspectral and
758 thermal imagery. *Remote Sens.* 8. <https://doi.org/10.3390/rs8040276>

759 Martin, M.E., Plourde, L.C., Ollinger, S. V, Smith, M.-L., Mcneil, B.E., 2008. A generalizable method for
760 remote sensing of canopy nitrogen across a wide range of forest ecosystems. *Remote Sens.*
761 *Environ.* 112, 3511–3519. <https://doi.org/10.1016/j.rse.2008.04.008>

762 Mattheck, C., Breloer, H., 1994. Field guide for visual tree assessment (VTA). *Arboric. J.* 18, 1–23.
763 <https://doi.org/10.1080/03071375.1994.9746995>

764 Meerdink, S.K., Roberts, D.A., King, J.Y., Roth, K.L., Dennison, P.E., Amaral, C.H., Hook, S.J., 2016.
765 Linking seasonal foliar traits to VSWIR-TIR spectroscopy across California ecosystems. *Remote*
766 *Sens. Environ.* 186, 322–338. <https://doi.org/10.1016/j.rse.2016.08.003>

767 Merzlyak, M.N., Gitelson, A.A., Chivkunova, O.B., Rakitin, V.Y., 1999. Non-destructive optical
768 detection of leaf senescence and fruit ripening. *Physiol. Plant* 106, 135.

769 Morsdorf, F., Kötz, B., Meier, E., Itten, K.I., Allgöwer, B., 2006. Estimation of LAI and fractional cover
770 from small footprint airborne laser scanning data based on gap fraction. *Remote Sens. Environ.*
771 104, 50–61. <https://doi.org/10.1016/j.rse.2006.04.019>

772 Nowak, D.J., McHale, P.J., Ibarra, M., Crane, D., Stevens, J.C., Luley, C.J., 1998. Modeling the Effects of
773 Urban Vegetation on Air Pollution, in: *Air Pollution Modeling and Its Application XII*. Springer
774 US, Boston, MA, pp. 399–407. https://doi.org/10.1007/978-1-4757-9128-0_41

775 O’Neil-Dunne, J., MacFaden, S., Royar, A., 2014. A versatile, production-oriented approach to high-
776 resolution tree-canopy mapping in urban and suburban landscapes using GEOBIA and data
777 fusion. *Remote Sens.* 6, 12837–12865. <https://doi.org/10.3390/rs61212837>

778 Oshio, H., Asawa, T., Hoyano, A., Miyasaka, S., 2015. Estimation of the leaf area density distribution
779 of individual trees using high-resolution and multi-return airborne LiDAR data. *Remote Sens.*
780 *Environ.* 166, 116–125. <https://doi.org/10.1016/j.rse.2015.05.001>

781 Penuelas, J., Baret, F., Filella, I., 1995. Semi-empirical indices to assess carotenoids/chlorophyll a ratio
782 from leaf spectral reflectance. *Photosynthetica*.

783 Plowright, A.A., Coops, N.C., Chance, C.M., Sheppard, S.R.J., Aven, N.W., 2017. Multi-scale analysis of
784 relationship between imperviousness and urban tree height using airborne remote sensing.
785 *Remote Sens. Environ.* 194, 391–400. <https://doi.org/10.1016/j.rse.2017.03.045>

786 Porra, R., 2002. The chequered history of the development and use of simultaneous equations for
787 the accurate determination of chlorophylls *a* and *b*. *Photosynth. Res.* 73, 149–156.
788 <https://doi.org/10.1023/a:1020470224740>

789 Reitberger, J., Schnörr, C., Krzystek, P., Stilla, U., 2009. 3D segmentation of single trees exploiting full
790 waveform LIDAR data. *ISPRS J. Photogramm. Remote Sens.* 64, 561–574.
791 <https://doi.org/10.1016/j.isprsjprs.2009.04.002>

792 Rouse, J.W., Hass, R.H., Schell, J.A., Deering, D.W., 1973. Monitoring vegetation systems in the great
793 plains with ERTS. *Third Earth Resour. Technol. Satell. Symp.* 1, 309–317.
794 <https://doi.org/citeulike-article-id:12009708>

795 Royle, D.D., Lathrop, R.G., 1997. Monitoring Hemlock Forest Health in New Jersey Using Landsat TM
796 Data and Change Detection Techniques. *For. Sci.* 43, 327–335.
797 <https://doi.org/10.1093/forestscience/43.3.327>

798 Salmond, J.A., Tadaki, M., Vardoulakis, S., Arbuthnott, K., Coutts, A., Demuzere, M., Dirks, K.N.,
799 Heaviside, C., Lim, S., Macintyre, H., McInnes, R.N., Wheeler, B.W., 2016. Health and climate
800 related ecosystem services provided by street trees in the urban environment. *Environ. Heal.*
801 15, 36. <https://doi.org/10.1186/s12940-016-0103-6>

802 Sanders, J.R., Grabosky, J.C., 2014. 20 years later: Does reduced soil area change overall tree growth?
803 *Urban For. Urban Green.* 13, 295–303. <https://doi.org/10.1016/j.ufug.2013.12.006>

804 Sari, N.M., Kushardono, D., 2016. Quality Analysis of Single Tree Object With Obia and Vegetation

805 Index From Lapan Surveillance Aircraft Multispectral Data in Urban Area. *Geopanning J.*
806 *Geomatics Plan.* 3, 93. <https://doi.org/10.14710/geopanning.3.2.93-106>

807 Scharenbroch, B.C., Carter, D., Bialecki, M., Fahey, R., Scheberl, L., Catania, M., Roman, L.A., Bassuk,
808 N., Harper, R.W., Werner, L., Siewert, A., Miller, S., Hutya, L., Raciti, S., 2017. A rapid urban site
809 index for assessing the quality of street tree planting sites. *Urban For. Urban Green.* 27, 279–
810 286. <https://doi.org/10.1016/j.ufug.2017.08.017>

811 Scharenbroch, B.C., Lloyd, J.E., Johnson-Maynard, J.L., 2005. Distinguishing urban soils with physical,
812 chemical, and biological properties. *Pedobiologia (Jena).* 49, 283–296.
813 <https://doi.org/10.1016/j.pedobi.2004.12.002>

814 Sims, D., Gamon, J., 2002. Relationship between leaf pigment content and spectral reflectance
815 across a wide range species, leaf structures and development stages. *Remote Sens. Environ.* 81,
816 337–354. [https://doi.org/10.1016/S0034-4257\(02\)00010-X](https://doi.org/10.1016/S0034-4257(02)00010-X)

817 Singh, A., Serbin, S.P., McNeil, B.E., Kingdon, C.C., Townsend, P.A., 2015. Imaging spectroscopy
818 algorithms for mapping canopy foliar chemical and morphological traits and their uncertainties.
819 *Ecol. Appl.* 25, 2180–2197. <https://doi.org/10.1890/14-2098.1>

820 Somers, B., Cools, K., Delalieux, S., Stuckens, J., Van der Zande, D., Verstraeten, W.W., Coppin, P.,
821 2009a. Nonlinear Hyperspectral Mixture Analysis for tree cover estimates in orchards. *Remote*
822 *Sens. Environ.* 113, 1183–1193. <https://doi.org/10.1016/j.rse.2009.02.003>

823 Somers, B., Delalieux, S., Verstraeten, W.W., Coppin, P., 2009b. A Conceptual Framework for the
824 Simultaneous Extraction of Sub-pixel Spatial Extent and Spectral Characteristics of Crops.
825 *Photogramm. Eng. Remote Sens.* 75, 57–68. <https://doi.org/10.14358/PERS.75.1.57>

826 Somers, B., Tits, L., Coppin, P., 2014. Quantifying nonlinear spectral mixing in vegetated areas:
827 Computer simulation model validation and first results. *IEEE J. Sel. Top. Appl. Earth Obs.*
828 *Remote Sens.* 7, 1956–1965. <https://doi.org/10.1109/JSTARS.2013.2289989>

829 Sterckx, S., Vreys, K., Biesemans, J., Iordache, M.-D., Bertels, L., Meuleman, K., 2016. Atmospheric
830 correction of APEX hyperspectral data. *Misc. Geogr.* 20, 16–20. [https://doi.org/10.1515/mgrsd-](https://doi.org/10.1515/mgrsd-2015-0022)
831 2015-0022

832 Stone, C., Coops, N., Culvenor, D., 2000. Conceptual Development of a Eucalypt Canopy Condition
833 Index Using High Resolution Spatial and Spectral Remote Sensing Imagery. *J. Sustain. For.* 11,
834 23–45. https://doi.org/10.1300/J091v11n04_02

835 Stuckens, J., Somers, B., Delalieux, S., Verstraeten, W.W., Coppin, P., 2009. The impact of common
836 assumptions on canopy radiative transfer simulations: A case study in Citrus orchards. *J. Quant.*
837 *Spectrosc. Radiat. Transf.* 110, 1–21. <https://doi.org/10.1016/J.JQSRT.2008.09.001>

838 Thenkabail, P.S., Smith, R.B., De Pauw, E., 2000. Hyperspectral Vegetation Indices and Their
839 Relationships with Agricultural Crop Characteristics. *Remote Sens. Environ.* 71, 158–182.
840 [https://doi.org/10.1016/S0034-4257\(99\)00067-X](https://doi.org/10.1016/S0034-4257(99)00067-X)

841 Tits, L., Somers, B., Coppin, P., 2012. The potential and limitations of a clustering approach for the
842 improved efficiency of multiple endmember spectral mixture analysis in plant production
843 system monitoring. *IEEE Trans. Geosci. Remote Sens.* 50, 2273–2286.
844 <https://doi.org/10.1109/TGRS.2011.2173696>

845 Tits, L., Somers, B., Saeys, W., Coppin, P., 2014. Site-Specific Plant Condition Monitoring Through
846 Hyperspectral Alternating Least Squares Unmixing. *IEEE J. Sel. Top. Appl. Earth Obs. Remote*
847 *Sens.* 7, 3606–3618. <https://doi.org/10.1109/JSTARS.2014.2313984>

- Tits, L., Somers, B., Stuckens, J., Farifteh, J., Coppin, P., 2013. Integration of in situ measured soil status and remotely sensed hyperspectral data to improve plant production system monitoring: Concept, perspectives and limitations. *Remote Sens. Environ.* 128, 197–211. <https://doi.org/10.1016/J.RSE.2012.10.006>
- Townsend, P.A., Foster, J.R., Chastian Jr, R.A., Currie, W.S., 2003. Canopy nitrogen in the forests of the Central Appalachian Mountains using Hyperion and AVIRIS. *IEEE Trans. Geosci. Remote Sens.* 41, 1347–1354. <https://doi.org/Doi 10.1109/Tgrs.2003.813205>
- van Beek, J., Tits, L., Somers, B., Deckers, T., Janssens, P., Coppin, P., 2015. Reducing background effects in orchards through spectral vegetation index correction. *Int. J. Appl. Earth Obs. Geoinf.* 34, 167–177. <https://doi.org/10.1016/j.jag.2014.08.009>
- Van De Voorde, T., Vlaeminck, J., Canters, F., 2008. Comparing different approaches for mapping urban vegetation cover from landsat ETM+ data: A case study on brussels. *Sensors* 8, 3880–3902. <https://doi.org/10.3390/s8063880>
- Vogelmann, J.E., Rock, B.N., Moss, D.M., 1993. Red edge spectral measurements from sugar maple leaves. *Int. J. Remote Sens.* 14, 1563–1575. <https://doi.org/10.1080/01431169308953986>
- Vreys, K., Iordache, M.D., Biesemans, J., Meuleman, K., 2016. Geometric correction of APEX hyperspectral data. *Misc. Geogr.* 20, 11–15. <https://doi.org/10.1515/mgrsd-2016-0006>
- Wang, J., Sammis, T.W., Gutschick, V.P., Gebremichael, M., Dennis, S.O., Harrison, R.E., 2010. Review of satellite remote sensing use in forest health studies. *Open Geogr. J.* 3, 28–42. <https://doi.org/10.2174/1874923201003010028>
- Wang, Q., Li, P., 2012. Hyperspectral indices for estimating leaf biochemical properties in temperate deciduous forests: Comparison of simulated and measured reflectance data sets. *Ecol. Indic.* 14, 56–65. <https://doi.org/10.1016/j.ecolind.2011.08.021>
- Wirion, C., Bauwens, W., Verbeiren, B., 2017. Location- and Time-Specific Hydrological Simulations with Multi-Resolution Remote Sensing Data in Urban Areas. *Remote Sens.* 9, 645. <https://doi.org/10.3390/rs9070645>
- Xiao, Q., McPherson, E.G., 2005. Tree health mapping with multispectral remote sensing data at UC Davis, California. *Urban Ecosyst.* 8, 349–361. <https://doi.org/10.1007/s11252-005-4867-7>
- Xiao, Q., McPherson, E.G., Ustin, S.L., Grismer, M.E., 2000. A new approach to modeling tree rainfall interception. *J. Geophys. Res.* 105, 29173–29188. <https://doi.org/10.1029/2000JD900343>
- Zarco-Tejada, P.J., Miller, J.R., Noland, T.L., Mohammed, G.H., Sampson, P.H., 2001. Scaling-up and model inversion methods with narrowband optical indices for chlorophyll content estimation in closed forest canopies with hyperspectral data. *IEEE Trans. Geosci. Remote Sens.* 39, 1491–1507. <https://doi.org/10.1109/36.934080>
- Zhao, Y., Hao, Y., Zhen, Z., Quan, Y., 2017. A Region-Based Hierarchical Cross-Section Analysis for Individual Tree Crown Delineation Using ALS Data. *Remote Sens.* 9, 1084. <https://doi.org/10.3390/rs9101084>
- Zhen, Z., Quackenbush, L.J., Zhang, L., 2016. Trends in automatic individual tree crown detection and delineation-evolution of LiDAR data. *Remote Sens.* 8, 1–26. <https://doi.org/10.3390/rs8040333>

Supplement I

Detailed workflow in LAsTools software to create Canopy Height Model (CHM) from LiDAR point cloud data

The raw lidar point cloud was found to contain some error points (unrealistic low or high z-values). Therefore, we first clean this up using lasnoise.

```
lasnoise -i G:\...\*.las -step_xy 8 -step_z 2 -isolated 40 -odir G:\...\lasnoise\
```

The CHM has been created using lasground_new in combination with on-the-fly buffering. The latter significantly reduces the error around the edges of the individual tiles. More information can be found on: <http://rapidlasso.com/2015/08/07/use-buffers-when-processing-lidar-in-tiles/>

```
lasindex -i G:\...\lasnoise\*.las
```

We used the -metro option to create lasground. Class 7 (= noise) is ignored.

```
lasground_new -i G:\...\lasnoise\*.las -buffered 25 -remain_buffered -odir G:\...\lasground\ -cores 6 -ignore_class 7 -metro
```

```
lasheight -i G:\...\lasground\*.las -remain_buffered -odir G:\...\lasheight\ -replace_z -drop_below -2 -drop_above 100 -drop_class 7 -cores 6
```

```
lasgrid -i G:\...\lasheight\*.las -step 0.25 -highest -mem 2000 -cores 6 -fill 5 -otif -odir G:\...\lasgrid_metro\ -use_orig_bb
```

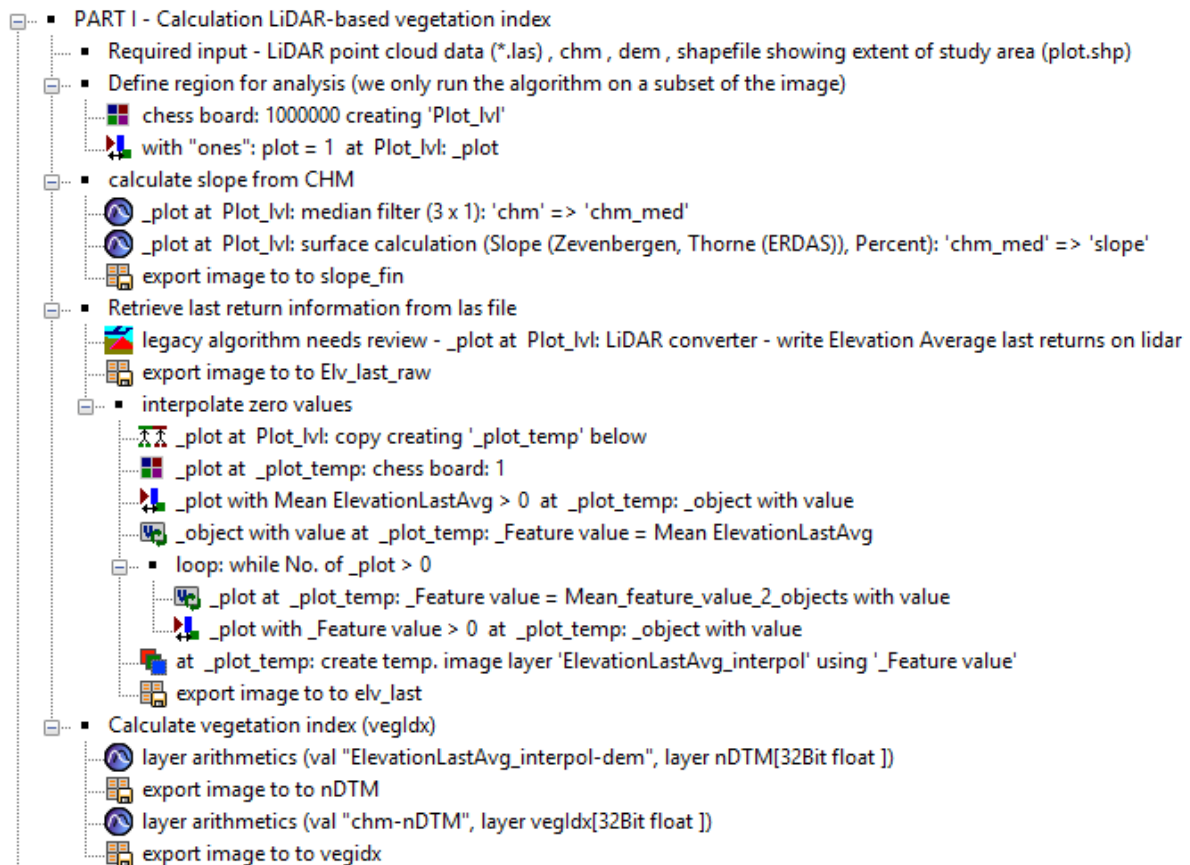
We also created a DTM, based on lasground:

```
blast2dem -i G:\...\lasground\*.las -otif -odir G:\...\dem\ -elevation -use_orig_bb -keep_class 2 -step 0.25 -cores 6
```

After these operations in LAsTools, all separate tiles were merged together using georeferenced mosaicking in ENVI classic 5.2. The resulting raster was imported in QGIS and saved as Geotiff.

Supplement II

eCognition ruleset for identifying and delineating individual tree crowns





922

923

924

Supplement III

Detailed results on effect of canopy pixel selection on accuracy of chlorophyll and LAI retrieval

Table III.1: Accuracy of chlorophyll retrieval in function of canopy pixel selection (n = 102). 1 = all pixels included, 2 = border pixels removed, 3 = pixels with NDVI lower than 0.3 removed, 4 = pixels with grass index lower than 0.87 removed, 5 = shaded pixels (brightness lower than 75% of maximum canopy brightness) removed. Highest accuracies per method are indicated in bold.

| | R ² | | | | | RMSE | | | | |
|-----------|----------------|-------------|-------------|-------------|-------------|------|------|------|------|------|
| | 1 | 2 | 3 | 4 | 5 | 1 | 2 | 3 | 4 | 5 |
| CARI | 0.22 | 0.21 | 0.30 | 0.31 | 0.31 | 12.1 | 12.6 | 10.0 | 9.7 | 9.6 |
| Cgreen | 0.37 | 0.39 | 0.39 | 0.40 | 0.39 | 8.6 | 8.2 | 8.1 | 8.0 | 8.1 |
| Cirededge | 0.40 | 0.41 | 0.41 | 0.42 | 0.42 | 8.0 | 7.8 | 7.8 | 7.7 | 7.8 |
| GitGreen | 0.20 | 0.27 | 0.29 | 0.31 | 0.28 | 13.1 | 10.8 | 10.1 | 9.7 | 10.3 |
| GitRed | 0.21 | 0.28 | 0.29 | 0.32 | 0.29 | 12.4 | 10.5 | 10.1 | 9.5 | 10.2 |
| 1DL_DGVI | 0.03 | 0.04 | 0.03 | 0.03 | 0.03 | 34.4 | 29.3 | 32.5 | 30.7 | 34.8 |
| MCARI | 0.21 | 0.19 | 0.29 | 0.31 | 0.31 | 12.4 | 13.3 | 10.3 | 9.7 | 9.7 |
| mND705 | 0.40 | 0.42 | 0.41 | 0.43 | 0.42 | 8.1 | 7.7 | 7.8 | 7.5 | 7.8 |
| mSR705 | 0.39 | 0.40 | 0.38 | 0.40 | 0.39 | 8.2 | 7.9 | 8.3 | 8.1 | 8.2 |
| MTCI | 0.46 | 0.45 | 0.46 | 0.46 | 0.46 | 7.1 | 7.3 | 7.1 | 7.1 | 7.1 |
| NAOC | 0.18 | 0.25 | 0.27 | 0.29 | 0.26 | 14.3 | 10.9 | 11.8 | 11.0 | 13.3 |
| ND680 | 0.02 | 0.04 | 0.04 | 0.04 | 0.01 | 35.0 | 28.6 | 28.6 | 28.0 | 46.8 |
| ND705 | 0.24 | 0.30 | 0.35 | 0.37 | 0.33 | 11.7 | 10.0 | 8.9 | 8.4 | 9.2 |
| NDRE | 0.32 | 0.38 | 0.40 | 0.41 | 0.39 | 9.4 | 8.4 | 8.1 | 7.9 | 8.2 |
| NDVI | 0.02 | 0.04 | 0.04 | 0.04 | 0.01 | 37.7 | 30.1 | 29.9 | 29.2 | 51.3 |
| PRI | 0.13 | 0.17 | 0.17 | 0.18 | 0.15 | 16.6 | 14.4 | 14.4 | 13.7 | 15.1 |
| PSRI | 0.01 | 0.02 | 0.01 | 0.01 | 0.00 | 42.9 | 35.3 | 51.4 | 47.8 | 68.8 |
| REP | 0.44 | 0.43 | 0.44 | 0.44 | 0.44 | 7.4 | 7.5 | 7.4 | 7.4 | 7.4 |
| RGRI | 0.00 | 0.00 | 0.01 | 0.02 | 0.05 | 59.0 | 84.3 | 43.6 | 37.9 | 26.9 |
| SIPI | 0.02 | 0.02 | 0.03 | 0.04 | 0.02 | 35.5 | 37.1 | 32.7 | 29.5 | 38.7 |
| SR680 | 0.03 | 0.06 | 0.06 | 0.06 | 0.04 | 31.2 | 24.4 | 24.1 | 23.6 | 28.9 |
| SR705 | 0.26 | 0.33 | 0.34 | 0.37 | 0.34 | 11.0 | 9.4 | 9.0 | 8.5 | 9.0 |
| VOG1 | 0.33 | 0.38 | 0.39 | 0.41 | 0.39 | 9.3 | 8.3 | 8.1 | 7.9 | 8.2 |
| VOG2 | 0.37 | 0.40 | 0.40 | 0.41 | 0.40 | 8.5 | 8.0 | 8.0 | 7.8 | 7.9 |
| VOG3 | 0.37 | 0.40 | 0.40 | 0.41 | 0.40 | 8.6 | 8.0 | 8.1 | 7.9 | 8.0 |
| DDn | 0.24 | 0.32 | 0.33 | 0.34 | 0.32 | 11.6 | 9.4 | 9.4 | 9.1 | 9.5 |
| Z-M | 0.32 | 0.38 | 0.39 | 0.41 | 0.40 | 9.5 | 8.4 | 8.1 | 7.8 | 8.0 |
| OMNBR | 0.38 | 0.41 | 0.42 | 0.46 | 0.43 | 8.3 | 7.8 | 7.6 | 7.0 | 7.5 |
| PLSR | 0.75 | 0.77 | 0.78 | 0.77 | 0.76 | 2.8 | 2.8 | 2.7 | 2.8 | 2.8 |
| PLSR_spp | 0.82 | 0.86 | 0.84 | 0.83 | 0.81 | 2.5 | 2.3 | 2.4 | 2.4 | 2.5 |

Table III.2: Accuracy of Leaf Area Index retrieval in function of canopy pixel selection (n = 102). 1 = all pixels included, 2 = border pixels removed, 3 = pixels with NDVI lower than 0.3 removed, 4 = pixels with grass index lower than 0.87 removed, 5 = shaded pixels (brightness lower than 75% of maximum canopy brightness) removed. Highest accuracies per method are indicated in bold.

| | R ² | | | | | RMSE | | | | |
|----------|----------------|-------------|------|-------------|-------------|------|-----|-----|-----|-----|
| | 1 | 2 | 3 | 4 | 5 | 1 | 2 | 3 | 4 | 5 |
| ARVI | 0.10 | 0.07 | 0.11 | 0.14 | 0.11 | 3.1 | 3.7 | 2.9 | 2.6 | 3.0 |
| EVI | 0.19 | 0.12 | 0.14 | 0.19 | 0.25 | 2.2 | 2.8 | 2.6 | 2.2 | 1.9 |
| 1DL_DGVI | 0.19 | 0.12 | 0.13 | 0.18 | 0.27 | 2.2 | 2.8 | 2.8 | 2.3 | 1.8 |
| NDVI | 0.11 | 0.07 | 0.12 | 0.14 | 0.12 | 3.0 | 3.7 | 2.8 | 2.6 | 2.8 |
| SAVI | 0.19 | 0.12 | 0.15 | 0.20 | 0.25 | 2.2 | 2.8 | 2.5 | 2.1 | 1.8 |
| sLAIDi | 0.20 | 0.15 | 0.13 | 0.16 | 0.27 | 2.1 | 2.5 | 2.7 | 2.4 | 1.8 |
| SR | 0.12 | 0.08 | 0.09 | 0.11 | 0.10 | 2.8 | 3.4 | 3.3 | 2.9 | 3.1 |
| VARI | 0.04 | 0.01 | 0.01 | 0.02 | 0.01 | 4.7 | 7.3 | 7.8 | 6.0 | 7.7 |
| Vlgreen | 0.04 | 0.01 | 0.00 | 0.01 | 0.01 | 4.8 | 8.9 | 9.5 | 7.1 | 8.3 |
| OMNBR | 0.28 | 0.29 | 0.30 | 0.35 | 0.33 | 1.7 | 1.7 | 1.6 | 1.5 | 1.5 |
| PLSR | 0.67 | 0.68 | 0.66 | 0.65 | 0.66 | 0.4 | 0.5 | 0.5 | 0.5 | 0.5 |
| PLSR_spp | 0.74 | 0.78 | 0.76 | 0.75 | 0.74 | 0.4 | 0.4 | 0.4 | 0.4 | 0.4 |

Supplement IV

Detailed results of comparison RS based vs VTA based tree health assessment per tree species

ACER (n = 19)

| Metric | Defoliation | Discoloration | Damage |
|---------------------|-------------|---------------|-------------|
| Total accuracy | 0.47 | 0.58 | 0.53 |
| Kappa | 0.27 | 0.30 | 0.36 |
| PA / UA class 0 | 0.67 / 0.86 | 0.78 / 0.70 | 0.67 / 0.86 |
| PA / UA class 1 | 0.50 / 0.17 | 0.43 / 0.43 | 0.50 / 0.17 |
| PA / UA class 2 | 0.50 / 0.33 | 0.33 / 0.50 | 0.50 / 0.25 |
| PA / UA class 3 | 0 / - | - / - | 0.33 / 1 |
| PA / UA class 0 + 1 | 1 / 0.85 | 0.94 / 0.88 | 1 / 0.85 |
| PA / UA class 2 + 3 | 0.75 / 1 | 0.33 / 0.50 | 0.75 / 1 |
| n Δ class = 0 | 9 | 11 | 10 |
| n Δ class = 1 | 10 | 8 | 8 |
| n Δ class = 2 | 0 | 0 | 1 |
| n Δ class = 3 | 0 | 0 | 0 |
| n RS > visual | 3 | 3 | 3 |
| n RS < visual | 10 | 8 | 9 |

AESCULUS (n = 23)

| Metric | Defoliation | Discoloration | Damage |
|---------------------|-------------|---------------|-------------|
| Total accuracy | 0.61 | 0.48 | 0.65 |
| Kappa | 0.46 | 0.28 | 0.54 |
| PA / UA class 0 | 0.50 / 0.57 | 0.71 / 0.56 | 0.57 / 0.67 |
| PA / UA class 1 | 0.50 / 0.43 | 0.20 / 0.11 | 0.75 / 0.43 |
| PA / UA class 2 | 0.83 / 0.71 | 0.63 / 1 | 0.60 / 0.60 |
| PA / UA class 3 | 0.67 / 1 | 0 / - | 0.71 / 1 |
| PA / UA class 0 + 1 | 0.86 / 0.86 | 1 / 0.67 | 0.91 / 0.77 |
| PA / UA class 2 + 3 | 0.78 / 0.78 | 0.45 / 1 | 0.75 / 0.90 |
| n Δ class = 0 | 14 | 11 | 15 |
| n Δ class = 1 | 6 | 9 | 6 |
| n Δ class = 2 | 3 | 3 | 1 |
| n Δ class = 3 | 0 | 0 | 1 |
| n RS > visual | 5 | 2 | 4 |
| n RS < visual | 9 | 12 | 8 |

PLATANUS (n = 27)

| Metric | Defoliation | Discoloration | Damage |
|---------------------|-------------|---------------|-------------|
| Total accuracy | 0.67 | 0.59 | 0.56 |
| Kappa | 0.50 | 0.39 | 0.40 |
| PA / UA class 0 | 0.78 / 0.78 | 0.64 / 0.90 | 0.78 / 0.78 |
| PA / UA class 1 | 0.70 / 0.64 | 0.63 / 0.50 | 0.71 / 0.56 |
| PA / UA class 2 | 0.50 / 0.57 | 0.67 / 0.29 | 0.22 / 0.50 |
| PA / UA class 3 | - / - | 0 / - | 0.50 / 0.20 |
| PA / UA class 0 + 1 | 0.84 / 0.80 | 0.86 / 0.95 | 0.88 / 0.78 |
| PA / UA class 2 + 3 | 0.50 / 0.57 | 0.80 / 0.57 | 0.63 / 0.78 |
| n Δ class = 0 | 18 | 16 | 15 |
| n Δ class = 1 | 7 | 10 | 9 |
| n Δ class = 2 | 2 | 1 | 3 |
| n Δ class = 3 | 0 | 0 | 0 |
| n RS > visual | 5 | 7 | 7 |
| n RS < visual | 9 | 11 | 12 |

950

951 *TILIA* (n = 33)

| Metric | Defoliation | Discoloration | Damage |
|----------------------|-------------|---------------|-------------|
| Total accuracy | 0.67 | 0.70 | 0.70 |
| Kappa | 0.51 | 0.48 | 0.56 |
| PA / UA class 0 | 0.87 / 0.87 | 0.94 / 0.73 | 0.87 / 0.93 |
| PA / UA class 1 | 0.63 / 0.50 | 0.50 / 0.71 | 0.75 / 0.55 |
| PA / UA class 2 | 0.60 / 0.43 | 0.67 / 0.50 | 0 / 0 |
| PA / UA class 3 | 0.20 / 1 | 0 / - | 0.50 / 1 |
| PA / UA class 0 + 1 | 0.96 / 0.88 | 0.96 / 0.90 | 0.96 / 0.88 |
| PA / UA class 2 + 3 | 0.70 / 0.88 | 0.50 / 0.75 | 0.70 / 0.88 |
| n Δ class = 0 | 22 | 23 | 23 |
| n Δ class = 1 | 10 | 8 | 9 |
| n Δ class = 2 | 1 | 0 | 1 |
| n Δ class = 3 | 0 | 2 | 0 |
| n RS > visual | 3 | 2 | 3 |
| n RS < visual | 11 | 10 | 10 |

952

953

954